

The High Latitude Snowfall Detection and Estimation Algorithm for ATMS (HANDEL-ATMS): a new algorithm for the snowfall retrieval at high latitudes

Andrea Camplani¹, Daniele Casella¹, Paolo Sanò¹, Giulia Panegrossi¹

¹National Research Council of Italy, Institute of Atmospheric Sciences and Climate (CNR-ISAC), Via del Fosso del Cavaliere 100, 00133 Rome, Italy

Correspondence to: Andrea Camplani (Andrea.Camplani@artov.isac.cnr.it)

Abstract. Snowfall detection and quantification are challenging tasks in the Earth system science field. Ground-based instruments have limited spatial coverage and are scarce or absent at high latitudes. Therefore, the development of satellite-based snowfall retrieval methods is necessary for the global monitoring of snowfall. Passive Microwave (PMW) sensors can be exploited for snowfall quantification purposes because their measurements in the high-frequency channels (> 80 GHz) respond to snowfall microphysics. However, the highly non-linear PMW multichannel response to snowfall, the weakness of snowfall signature and the contamination by the background surface emission/scattering signal make snowfall retrieval very difficult. This phenomenon is particularly evident at high latitudes, where light snowfall events in extremely cold and dry environmental conditions are predominant. [Machine Learning \(ML\)](#) techniques have been demonstrated to be very suitable to handle the complex PMW multichannel relationship to snowfall. Operational microwave sounders on near-polar orbit satellites such as the Advanced Technology Microwave Sounder (ATMS), and the European MetOp-SG Microwave Sounder in the future, offer a very good coverage at high latitudes. Moreover, their wide range of channel frequencies (from 23 GHz to 190 GHz), allows for the [dynamic](#) radiometric characterization of the surface at the time of the overpass along with the exploitation of the high-frequency channels for snowfall retrieval. The paper describes the High Latitude Snow Detection and Estimation Algorithm for ATMS (HANDEL-ATMS), a new machine learning-based snowfall retrieval algorithm developed specifically for high latitude environmental conditions and based on the ATMS observations.

HANDEL-ATMS is based on the use of an observational dataset in the training phase, where each ATMS multichannel observation is associated with coincident (in time and space) CloudSat Cloud Profiling Radar (CPR) vertical snow profile and surface snowfall rate. The main novelty of the approach is the radiometric characterization of the background surface (including snow covered land and sea ice) at the time of the overpass to derive multi-channel surface emissivities and clear-sky contribution to be used in the snowfall retrieval process. The snowfall retrieval is based on four different artificial neural networks for snow water path (SWP) and surface snowfall rate (SSR) detection and retrieval. HANDEL-ATMS shows very good detection capabilities - POD = 0.83, FAR = 0.18, and HSS = 0.68 for the SSR detection module. Estimation error statistics show a good agreement with CPR snowfall products for $SSR > 10^{-2}$ mm h⁻¹ (RMSE 0.08 mm h⁻¹, bias=0.02 mm h⁻¹). The analysis of the results for an independent CPR dataset and of selected snowfall events evidence the unique capability of HANDEL-ATMS to detect and estimate SWP and SSR also in presence of extreme cold and dry environmental conditions typical of high latitudes.

1 Introduction

Snowfall retrieval is one important topic in the atmospheric science field. On a global scale, snowfall represents only 5 % of the total global precipitation but it is predominant above 60-70 ° N/S (see *Levizzani et al, 2011*). In recent years, several studies have highlighted the strong influence of global warming on snowfall distribution and regimes, especially at high latitudes (see *Liu et al, 2009, Liu et al, 2012, Bintanja & Selten, 2014, Vihma et al, 2015*). However, global snowfall quantification is a challenging topic in weather sciences. Ground-based instruments such as raingauges or snowgauges provide only punctual measurements which can not fully capture the spatial variability of precipitation phenomena; moreover, the variability of snowflake shape and density has a strong influence on their fall speed and trajectories and therefore gauge-based measurements of falling snow result to be less accurate than for rain (see *Skofronick-Jackson et al, 2015*). Weather radars can provide areal measurements of precipitation - the rate estimation is based on the conversion of the measured backscattered radiation to precipitating hydrometeors content - but such operation presents some technical limitations (see *Kidd*

49 & Huffman, 2011). Finally, most of the regions where snowfall is predominant - such as Greenland, Siberia,
50 Canada, and Antarctica - are uninhabited or otherwise sparsely populated areas where weather observation
51 networks are very scarce or totally absent. Therefore, the development of satellite-based methods for snowfall
52 retrieval is necessary for global monitoring of snowfall. Passive Microwave (PMW) sensors on board polar
53 orbiting satellites can be exploited for snowfall detection purposes because the microwave (MW) signal is directly
54 responsive to the spatial distribution and microphysics properties of precipitation-sized hydrometeors in the
55 clouds; at the same time, the use of PMW sensors guarantees a high spatial coverage and high temporal resolution
56 (see Kidd & Huffman, 2011).

57 PMW snowfall detection and quantification is typically based on the ability to interpret the snowfall scattering
58 signature in the high frequency channels (> 90 GHz), which respond more effectively to ice microphysics and are
59 less prone to surface effects than low frequency channels, and to distinguish it from the clear-sky (surface and
60 atmosphere) contribution (e.g., Panegrossi et al., 2017). However, several factors make the PMW snowfall signal
61 ambiguous and the relationship between multichannel measurements and surface snowfall intensity highly non-
62 linear, especially in extremely cold/dry environmental conditions (see Panegrossi et al., 2022). The snowfall
63 scattering signal is relatively weak and is highly dependent on the complex microphysical properties of snowflakes
64 (Kim et al., 2008, Kulie et al., 2010, Kongoli et al., 2015), it is often masked by supercooled liquid water emission
65 signal (Wang et al., 2013, Battaglia & Delanoë, 2013, Panegrossi et al., 2017, Rysman et al., 2018, Battaglia &
66 Panegrossi, 2020, Panegrossi et al., 2022), and can be contaminated by the extremely variable background surface
67 emissivity (Liu and Seo, 2013, Takbiri et al., 2019, Rahimi et al., 2017), especially in cold and dry conditions
68 typical of the high latitude regions (Camplani et al., 2021). In this context, the availability of the ~~last~~ latest
69 generation microwave radiometers - such as the conically-scanning radiometer GPM Microwave Imager (GMI)
70 and the cross-track scanning radiometer Advanced Technology Microwave Sensor (ATMS) - whose channels
71 cover a wide range of frequencies - offers new possibilities for global snowfall monitoring. The multi-channel
72 PMW observations can be used for both a [dynamic](#) radiometric characterization of the background surface - using
73 the low-frequency channels (< 90 GHz) - and for the detection and the estimation of the snowfall using the high-
74 frequency channels (> 90 GHz) (see Panegrossi et al., 2022).

75 The PMW capability to characterize physically and radiometrically the background surface varies from sea to
76 land, especially for the identification of cold/frozen surfaces. For what concerns the ocean, sea ice detection using
77 PMW observations has been a well-documented topic in the remote sensing science field since the 70s. This is
78 due to the strong contrast between sea ice (≈ 0.9) and open water (≈ 0.5) emissivity values at the MW low-
79 frequency range (~ 19 GHz) (see Comiso, 1983). Other studies highlighted the ability to discriminate between
80 different types of ice using a set of low-frequency window channels, because the differences between the
81 emissivities of the different types of sea ice increase with increasing frequency; in particular, at higher frequencies
82 (30-50 GHz) the contrast between the emissivity of “new” ice and “old” ice increases, with a decrease of the
83 emissivity at higher frequencies for “older” sea ice (see Comiso, 1983, Ulaby et al. & Long, 2014). Moreover, it
84 has been observed that the simultaneous presence of open water and sea ice causes a decrease in the low-frequency
85 channel emissivity; the observed emissivity can be considered as a linear combination of the emissivity spectra of
86 sea ice and open water (see Ulaby et al. & Long, 2014). For what concerns continental areas, the detection of
87 snow-covered land surfaces using MW [measurements](#) results to be more difficult. In dry conditions, a snowpack
88 acts as a volume scatterer; the scattering effect is dependent on the grain size and shape and on the depth of the
89 snowpack (see Clifford, 2010). However, the presence of liquid water can mask the scattering signature (see
90 Mätzler & Hüppi, 1989). At the same time, large areas of Greenland and Antarctica ~~could appear as “scatter-~~
91 ~~free”, although these areas throughout the year are, while~~ covered by dry snowpacks [throughout the](#)
92 [year, do not show a significant difference between the two ATMS low frequency channels](#). Finally, some snow-
93 free areas, such as rocky mountains and cold deserts, present a scattering signature very similar to that of the
94 snowpack (see Grody & Basist, 1996). Therefore, the detection of snow-covered areas is very complex. A set of
95 several tests, each of which identifies snowpacks characterized by different physical and radiometric
96 characteristics, may be used.

97 This paper describes the development of a machine learning-based algorithm for snowfall retrieval (the High
98 Latitude sNowfall Detection and Estimation aLgorithm for ATMS, HANDEL-ATMS), exploiting ATMS
99 radiometer multi-channel measurements and using the CloudSat Cloud Profiling Radar (CPR) snowfall products

100 as reference. The algorithm has been developed focusing on the typical conditions of high latitude regions - low
101 humidity, low temperature, presence of snowpack on land or sea ice over ocean, and light snowfall intensity.
102 The main novelty of the approach is the exploitation of the ATMS wide range of channels (from 22 GHz to 183
103 GHz) to ~~obtain~~obtain the dynamic radiometric characterization of the background surface at the time of the
104 overpass. The derived surface emissivities are used to infer the clear-sky contribution to the measured TBs in the
105 high-~~frequency channels in the snowfall retrieval process.~~ frequency channels in the snowfall retrieval
106 process. This approach is similar to the work of Zhao and Weng, 2002, for AMSU observations limited to non-
107 scattering surfaces (i.e., ocean and vegetated land), however the application to surfaces with a very complex and
108 time-varying emissivity (such as snow cover and sea ice) required a far-away more advanced algorithm taking
109 advantage of machine learning techniques. Moreover, the algorithm is based on the exploitation of an
110 observational dataset where each ATMS multichannel observation is associated with coincident (in time and
111 space) CloudSat CPR vertical snow profile and surface snowfall rate (hereafter ATMS-CPR coincidence dataset).
112 Several snowfall retrieval algorithms for cross-track scanning radiometers have evolved in the last 20 years
113 starting from the Advanced Microwave Sounder Unit-B (AMSU-B) (*Zhao and Weng, 2002, Kongoli et al, 2003,*
114 *Skofronick-Jackson et al, 2004, Noh et al., 2009, Liu and Seo 2013*), and Microwave Humidity Sounder (MHS)
115 (see *Liu & Seo, 2013, Edel et al, 2020*), and evolving to ATMS (*Kongoli et al, 2015, Meng et al, 2017, Kongoli*
116 *et al, 2018, You et al, 2022, Sanò et -al, 2022*). Some of them are based on radiative transfer simulations of
117 observed snowfall events (*Kongoli et al, 2003, Skofronick-Jackson et al, 2004, Kim et al, 2008*), or on in-situ data
118 (see *Kongoli et al, 2015, Meng et al, 2017, Kongoli et al, 2018*), others on CPR observations (*Edel et al, 2020,*
119 *You et al, 2022, Sanò et -al, 2022*), or a combination of them (*Noh et al, 2009, Liu & Seo, 2013*).- In the last five
120 years, there has been an increasing use of machine learning (ML) approaches trained on CPR-based coincidence
121 datasets. These approaches have proven to be very effective for snowfall retrieval. On one side, ML techniques
122 are suitable to handle the complex, ~~nonlinear~~non-linear PMW multichannel response to snowfall (e.g., *Rysman*
123 *et al., 2018, Edel et al., 2020, Sanò et al., 2022*). On the other ~~side~~hand, the use of CPR-based datasets
124 overcomes some of the limitations deriving from the ~~assumptions to be made in use of~~ cloud-radiation
125 model simulations ~~(e. g., the microphysics scheme, the emissivity of the background surface,~~
126 ~~scattering properties of ice hydrometeors),~~ which are particularly ~~problematic~~challenging for snowfall
127 ~~estimation~~events. However, some limitations of the radar product used as ~~a~~ reference and issues related to the
128 spatial and temporal matching between the CPR and the PMW radiometer measurements ~~introduces some~~
129 ~~uncertainty.~~ introduce some uncertainty. Moreover, the 2CSP product is based on assumptions on snow
130 microphysics, uses optimal estimation to retrieve snow parameters, and uses a simplified radar reflectivity
131 equation and is affected by CloudSat CPR limitations as outlined in Battaglia & Panegrossi, 2020.
132 For what concerns ATMS, the ML-based Snow retrieval ALgorithm fOr gpM-Cross Track (SLALOM-CT)
133 (*Sanò et al., 2022*) has been developed within the EUMETSAT Satellite ~~Application~~Application Facility for
134 Hydrology (H SAF) in preparation for the launch of the EPS-SG Microwave Sounder (MWS). Similarly to
135 HANDEL-ATMS, it is trained on a ATMS-CPR coincidence dataset. SLALOM-CT is the evolution for cross-
136 track scanning radiometers of the Snow retrieval ALgorithm fOr GMI (SLALOM) (*Rysman et al, 2018, Rysman*
137 *et al, 2019*) which was the first ML algorithm for snowfall detection and retrieval for GMI trained and tested on
138 GMI-CPR coincident observations made available in the NASA GPM-CloudSat coincidence dataset (*Turk et al.,*
139 *2021a*). One of the novelties in the SLALOM (SLALOM-CT) approach is the use of the GMI (ATMS) low-
140 frequency channels to better constrain the snowfall retrieval to the characteristics of the surface at the time of the
141 overpass (*Turk et al., 2021b*). SLALOM-CT is based on a modular scheme, i.e., four separate modules are used
142 for snowfall detection, supercooled water layer detection, snow water path (SWP) and surface snowfall rate (SSR)
143 estimate. The predictor set is composed of the ATMS TBs and some environmental variables (T_{2m} , TPW, and
144 principal components derived from temperature and humidity profiles).
145 However, none of the algorithms mentioned here were ~~trained~~tailored specifically ~~for~~to the extreme conditions
146 typical of high latitudes. The present work has the aim to develop an algorithm for snowfall detection and
147 estimation by exploiting the large frequency range typical of the last generation radiometers and to obtain a
148 dynamic radiometric characterization of the background surface at the time of the satellite overpass in order to
149 highlight the complex relationship between upwelling radiation and snowfall signature, which makes the detection
150 very difficult in the typical conditions of the high latitudes.

151 This article is organized as follows: Section 2 provides background information on ATMS and CPR, on the
152 methodology used to build the coincidence dataset and on the machine learning approaches used to develop the
153 algorithm. In Section 3 the algorithm structure is described. In Section 4 the overall performance scores are
154 reported and analyzed; a case study is analyzed and a comparison with SLALOM-CT is reported. Section 5 is
155 dedicated to the summary of the main results and to the conclusions.

156 2. Instruments and methods

157 2.1 Advanced Technology Microwave Sounder (ATMS)

158 ATMS is a total power cross-track scanning radiometer within 52.7° off the nadir direction. It has a total of 22
159 channels with the first 16 channels primarily used for temperature sounding from the surface to about 1 hPa (45
160 km) and the remaining channels used for water vapor sounding in the troposphere from the surface to about 200
161 hPa (10 km)-), and for cloud properties and precipitation retrieval. There are two receiving antennas: one serving
162 channels 1–15 below 60 GHz, and the other for channels above 60 GHz. The beamwidth changes with frequency
163 and is 5.2° for channels 1–2 (23.8–31.4 GHz), 2.2° for channels 3–16 (50.3–57.29 and 88.2 GHz), and 1.1° for
164 channels 17–22 (165.5–183.3 GHz). The corresponding nadir resolutions are 74.78, 31.64, and 15.82 km,
165 respectively. The outmost field of view (FOV) sizes are $323.1 \text{ km} \times 141.8 \text{ km}$ (cross-track \times along-track), 136.7
166 $\text{km} \times 60.0 \text{ km}$, and $68.4 \text{ km} \times 30.0 \text{ km}$, respectively. ~~The ATMS can be considered the evolution of the~~
167 ~~three main previous cross-track scanning radiometers: Advanced Microwave Sounding Unit-~~
168 ~~A (AMSU-A), Advanced Microwave Sounding Unit-B (AMSU-B), and Microwave Humidity~~
169 ~~Sounder (MHS). Seventeen ATMS channels (channels 1–3, 5–15, 17, 20, and 22) have the~~
170 ~~same frequencies as its two predecessors AMSU, two ATMS channels (channels 16 and 18)~~
171 ~~have slightly different frequencies from AMSU channels, and three new channels (channels~~
172 ~~4, 19 and 21) have been added to ATMS~~ (see *Weng et al, 2012*). ATMS is currently carried by three
173 near-polar orbiting satellites, Suomi National Polar-orbiting Partnership (SNPP) NOAA-20, and NOAA-21
174 providing global coverage including polar regions. ~~Moreover, each~~ Each satellite revisiting time is equal to 12
175 hours at the equator, but drops to 100 minutes over the polar regions, ensuring a very high temporal resolution for
176 the research area of interest in this work. Moreover, the operational nature of the mission guarantees observations
177 for the next decades. It is worth noticing that the polarization of ATMS channels is not defined as vertical or
178 horizontal, but as “Quasi-Vertical” or “Quasi-Horizontal”. The “Quasi” prefix is used to indicate that ATMS (and
179 any other cross-track scanner) measures vertical or horizontal polarization only when looking at nadir and a
180 mixture of V and H polarization for off-nadir scan angles.

181 2.2 Cloud Profiling Radar (CPR)

182 The CPR is a 94 GHz nadir-looking radar onboard CloudSat. CloudSat was launched on April 28, 2006; the W-
183 band (94 GHz) Cloud Profiling Radar (CPR) operations began on June 2, 2006. CPR has been acquiring the first-
184 ever continuous global time series of vertical cloud structures and vertical profiles of cloud liquid and ice water
185 content with a 485-m vertical resolution and a 1.4-km antenna 3-dB footprint. The reference CloudSat snowfall
186 product is the 2C-Snow-Profile (2CSP) product (Version 5 is used in this work). It provides estimates of snowfall
187 characteristics for each observed profile. In particular, it provides an estimate of the Snow Water Path (SWP), i.
188 e., the total snow water content integrated over the atmospheric column, and of the Surface Snowfall Rate (SSR)
189 (see *Stephens et al, 2008*). SWP is estimated also when there is no snowfall at the ground level; therefore, the
190 presence of SWP is not always linked to the ~~presence of~~ SSR, especially in warmer near-surface conditions
191 (see *Wood & L'Ecuyer, 2018*). 2CSP has several limitations, such as the contamination of the signal in the lowest
192 1000 - 1500 m of the profile due to ground-clutter, the underestimation of the heavy snowfall ~~events~~, due to
193 attenuation of the radar signal in these conditions, and the limited temporal sampling (although it is higher in the
194 polar regions), and the day-only operation mode since 2011, which limits its use during the winter seasons (see
195 *Milani and Wood, 2021, Panegrossi et al, 2022*). However, 2CSP has been demonstrated to be more accurate than
196 GPM Dual-frequency Precipitation Radar (DPR) snowfall products (see *Casella et al, 2017*) and in good
197 agreement with estimates obtained by ground-based radars (e.g., *Mroz et al, 2021*), although it is affected by
198 underestimation for medium-heavy snowfall events. Moreover, the polar orbit and the W-band high sensitivity
199 make CPR suitable for snowfall monitoring at higher latitudes (as demonstrated in several studies, *Kulie et al,*
200 *2016, Milani et al, 2018*) typically characterized by light/moderate intensity (*Beranghi et al, 2016*).

201 2.3 ATMS-CPR Coincidence Dataset

202 The present study is based on a coincidence dataset between CPR and [SNPP](#) ATMS observations between January
203 2014 and August 2016. The same dataset has been used for the development of SLALOM-CT (*Sanò et al, 2022*).
204 Each coincidence comes from observations from CloudSat CPR and ATMS - onboard SNPP - within a maximum
205 15-minute time window. Moreover, the elements in the dataset have been selected by removing all corrupted data
206 and by applying an additional filter based on the minimum distance between CPR and ATMS IFOV center which
207 (22 km). The zonal distribution of the coincidences is due to the orbital geometry of CloudSat and SNPP, which
208 are both sun-synchronous with a relatively small difference in the satellite height (i.-e., about 689 km and 833 km
209 for CloudSat and SNPP respectively). Therefore, the coincidence dataset is built from longer orbit fragments
210 (often semi-orbits) and by a very large number of elements near the poles. There is an asymmetry in the CPR
211 sampling between the Northern and the Southern hemisphere that can be observed in the dataset due to the CPR
212 daytime-only mode operation since 2011, which influences mostly the acquisitions in the Southern Polar region-
213 [\(Milani and Wood, 2021\)](#).

214 The database has been built considering the horizontal resolution of the high-frequency channels of ATMS. The
215 CPR snowfall product used as reference is the 2CSP (~~v.5V5~~). Some model-derived variables, [specifically Total](#)
216 [Precipitable Water \(TPW\), the 2-m Temperature \(\$T_{2m}\$ \), the Skin Temperature, the freezing level height and the](#)
217 [temperature and humidity profiles](#), have been added to the dataset to be used as ancillary ~~variables-parameters~~.
218 Both 2D and 3D environmental variables have been obtained from the European Center Medium Weather Forecast
219 (ECMWF). In particular, they are obtained from the CPR ECMWF-AUX product where the set of ancillary
220 ECMWF atmospheric state variable data is associated with each CloudSat CPR bin (the product is described by
221 *Partain, 2022*). Moreover, a cloud-cover fraction index, which indicates the fraction of CPR observations where
222 cloud is observed on the total CPR observations within each ATMS pixel, is added to the dataset.

223 Information about the presence of supercooled water is added in the coincidence dataset to be used towards the
224 correct interpretation of the snowfall signal in presence of supercooled water layers. The supercooled water
225 information has been extracted from the DARDAR product (see DARDAR). DARDAR, which stands for
226 raDAR+LiDAR, combines CPR radar and Cloud-Aerosol Lidar with Orthogonal Polarization (CALIOP) lidar
227 observations, onboard Cloud-Aerosol Lidar and Infrared Pathfinder Satellite Observations (CALIPSO) satellite,
228 and estimates both the cloud water phase and the ice water content and ice particle effective radius (see *Battaglia*
229 *& Delanoë, 2013, Ceccaldi et al, 2013*). In particular, the coincidence dataset includes an index indicating the
230 presence of supercooled [cloud](#) liquid water within each ATMS pixel, calculated as the fraction of DARDAR
231 observations where supercooled water within and on the top of the cloud is observed to the total DARDAR
232 observations within each pixel.

233 The association of ATMS TBs and CPR products has been done by averaging the CPR snow products with a
234 Gaussian function approximating the ATMS high-frequency antenna pattern (varying with the scan angle). It is
235 worth noting, however, that the ATMS IFOV is under-sampled by the narrow swath of the CPR (see *Sanò et al.,*
236 [2022 for details](#)), ~~2022 for details~~. ~~Moreover, it is worth noting that CPR 2CSP product limitations for~~
237 [snowfall detection and estimation \(see Section 2.2\) might affect the ATMS-based snowfall estimates.](#)

238 [In this work, the dataset has been filtered based on humidity \(\$TPW < 10\$ mm\), temperature \(\$T_{2m} < 280\$ K\) and](#)
239 [elevation conditions \(the working limits of the PESCA algorithm, see *Camplani et al, 2021*\) leading to a good](#)
240 [representation of the higher latitudes with 80 % of the dataset elements located above 60°N/S. The dataset is made](#)
241 [of \$2.14 \cdot 10^6\$ elements, including \$1.07 \cdot 10^6\$ elements with falling snow \(\$2CSP\ SWP > 0\ kg\ m^{-2}\$ \) and \$9.99 \cdot 10^5\$ with](#)
242 [snowfall at the surface \(\$2CSP\ SSR > 0\ mm\ h^{-1}\$ \). The training and test phases have been conducted by splitting](#)
243 [randomly the dataset, with \$\frac{1}{3}\$ of the elements in the training and \$\frac{2}{3}\$ of the elements in the test dataset.](#)

244 2.4 Machine Learning approaches

245 The algorithm is based on different machine-learning (ML) techniques. ~~These techniques are widely~~
246 ~~applied in Earth observation because of their ability to approximate, to an arbitrary degree of~~
247 ~~accuracy, complex nonlinear, and imperfectly known functions. A fundamental characteristic~~
248 ~~of these techniques is that the training process eliminates the need for a well-defined physical~~
249 ~~or numerical model that describes the relationships between the input values and output~~
250 ~~results, allowing the identification of these relationships during the learning phase (see *Sanò*~~
251 ~~*et al, 2022*).~~ Moreover, clustering techniques have been used to characterize from a radiometric point of view

252 the background surface. In particular, an unsupervised clustering technique has been used to identify emissivity
253 clusters with small internal variability, and a supervised clustering technique has been used to identify an
254 emissivity spectrum based on other parameters.

255 **2.4.1 Artificial Neural Networks**

256 ~~An Artificial Neural Network (ANN) is an information-processing system inspired by the~~
257 ~~functioning of biological neural networks. It is composed of neurons, i. e., elements where the~~
258 ~~information is processed using an activation function, and the connecting links between the~~
259 ~~neurons, where a weight multiplies the deriving from the upstream signal. In particular, the~~
260 ~~The~~ HANDEL-ATMS snowfall detection and estimation modules have been developed using feedforward multilayer
261 neural network architectures, i. e., a neural network architecture where the neurons are arranged in layers;
262 ~~each neuron belonging to a layer receives, as input to its transfer function, a weighted sum of the~~
263 ~~outputs of the previous layer.~~ This architecture, which is defined by the number of layers, the number of
264 neurons for each layer, and the transfer function of each neuron, has to be designed beforehand. The weights of
265 connection links and the bias values for each layer are estimated with a training process, based on the Levenberg–
266 Marquardt algorithm (see Sandò et al, 2015). [The specific networks architecture, and the training and optimization](#)
267 [procedure of the HANDEL-ATMS algorithm are described in detail in section 3.2.](#)

268 **2.4.2 Self Organizing Maps**

269 The unsupervised clustering method used for the background surface classification is the Self Organizing Map
270 (SOM) method (see [Kohonen, 2012](#)). ~~The characteristic of this method is to assume a topological~~
271 ~~structure among the cluster units: the maps can be represented as a neuron network where~~
272 ~~each neuron represents a cluster. Similar to the k-means clustering method, the neuron is~~
273 ~~associated with an input vector by minimizing a distance measurement; however, not only the~~
274 ~~weight vector of the winning neuron is updated, but also the weight vectors of all the neurons~~
275 ~~which are considered topologically close (see Faussett, 2006). Therefore,~~ [Faussett, 2006,](#)
276 [Kohonen, 2012](#)). ~~The characteristic of this method is that~~ classes that are close to each other from a topological
277 point of view can be considered similar also from a physical and radiometric point of view (see [Munchak et al,](#)
278 [2020](#)). SOMs have been ~~already used to make a in previous studies for the~~ classification of the background
279 surface by creating clusters based on emissivity values (see [Prigent et al, 2001](#), [Cordisco et al, 2006](#), [Prigent et](#)
280 [al, 2008](#), [Munchak et al, 2020](#)).

281 **2.4.3 Linear Discriminant Analysis**

282 Several supervised clustering methods have been tested in this study, such as the linear discriminant analysis, the
283 quadratic discriminant analysis, the classification tree, and the nearest neighbor method. The final choice came
284 down to linear discriminant analysis (LDA, [see Hastie et al, 2009](#)) because this method guarantees satisfactory
285 accuracy in the results with a difference between the performances of the training and the test phase which is not
286 too significant, and a computational effort which is not too high. ~~Discriminant Analyses are classification~~
287 ~~methods based on the assumption that each observation is a realization of a normal~~
288 ~~distribution – if there is a single predictor – or a multivariate normal distribution – if it is based~~
289 ~~on more than one predictor. In particular, LDA assumes that clusters have a common~~
290 ~~covariance analysis; therefore, the decision boundary between the clusters results to be linear~~
291 ~~relationships (see Hastie et al, 2009).~~

292 **3 Algorithm description**

293 The configuration of the HANDEL-ATMS is summarized in the Flowchart in Figure 1. The process begins with
294 the classification of the background surface using the PMW Empirical cold Surface Classification Algorithm
295 (PESCA, [Camplani et al, 2021](#)); then, the surface emissivity spectra are derived through refinement process based
296 on LDA and these are used to estimate clear-sky simulated TB (TB_{sim}) using the ECMWF-AUX atmospheric
297 temperature and water vapor profiles. Then, the differences between the TB_{sim} and the ATMS observed TB (TB_{obs})
298 are evaluated ($\Delta TB_{obs-sim} = TB_{obs} - TB_{sim}$). Four ANNs are then applied to a predictor set consisting of ATMS
299 TB_{obs} , $\Delta TB_{obs-sim}$, a surface classification flag, and other ~~environmental and~~ ancillary parameters- ([elevation](#)
300 [and ATMS viewing angle for the final version](#)). Finally, the pixels classified with the presence of snowfall by the

301 detection module, are used in the estimation modules while for no-snowfall flagged pixels the snowfall rate value
302 is set to 0 mm/h. In the following sections the main blocks of the algorithm are described in detail.

303 3.1 Surface Classification and emissivity spectra estimation

304 3.1.1 PESCA Design and Performances

305 The [dynamic](#) classification and radiometric characterization of the background surface at the time of the satellite
306 overpass is based on PESCA exploiting ATMS low-frequency channels ([Camplani et al., 2021](#)). The algorithm
307 discriminates between frozen and unfrozen surfaces (sea ice and open water, snow-covered land and snow-free
308 land), and identifies 10 surface classes (4 over ocean, 5 over land, 1 for coast). The algorithm has been tuned
309 against the [NASA/NOAA](#) AutoSnow product (see [Romanov, 2019](#)), which gives daily maps of sea ice and snow
310 cover. For each ATMS observation, a flag reporting the AutoSnow class percentage (sea ice, open water, snow-
311 covered land, snow-free land) has been calculated; then, a threshold has been applied to discriminate between sea
312 ice and open water pixels (sea ice AutoSnow class > 10 %) and between snow-covered and snow-free land pixels
313 (snow-covered land AutoSnow class > 50 %). ATMS pixels have been classified into land, ocean, and coast pixels
314 using a land-sea mask.

315 The land module discriminates between snow-free land and snow-covered land and identifies four different snow
316 cover classes (Perennial, Winter Polar, Thin, and Deep Dry). It is based on a decision tree that makes use of a
317 limited number of inputs (the ratio TB_{23QV}/TB_{31QV} - **ratio**, the difference between TB_{23QV} and TB_{88QV} or Scattering
318 Index - **SI**, 23 GHz pseudo-emissivity (i. e. the ratio between an observed brightness temperature (TB) and a near-
319 surface temperature value) - **pem₂₃**). The module has been described by [Camplani et al, 2021](#).

320 For what concerns the ocean module, a simple relationship to distinguish between sea ice and open water
321 observations has been identified. In Figure 2 a Cartesian plane where the x-axis represents 23 GHz observed
322 TB_{23QV} and the y-axis represents the near-surface temperature (T_{2m}) is shown. In the figure each point represents
323 a pseudo-emissivity value, and the color describes the mean AutoSnow sea ice percentage within each bin (see
324 Figure 2, left panel). It is possible to observe that open water (0 % of sea ice, blue) and sea ice (100 % of sea ice,
325 red) are characterized by very different pseudo-emissivities. ~~There is a~~ transition area between open water and
326 sea ice pseudo-emissivity values ~~can be observed: these values characterize for~~ IFOVs where both open
327 water and sea ice are present. The simple relationship for sea ice identification is reported in the left panel as a
328 green line where the condition for sea ice identification is defined by Equation 1.

$$329 TB_{23QV} > T_{2m} - 96 K$$

330 (1)

331 ~~The~~ [Downstream of the sea ice/open water identification, information about sea ice characteristics is obtained](#)
332 [from the](#) analysis of the two low-frequency pseudo-emissivity ~~values has been used to obtain information~~
333 ~~about sea ice characteristics downstream of the sea ice/open water identification. This is~~
334 ~~possible because~~ (**pem₂₃** and **pem₃₁**), which are a good approximation of sea-ice ~~surface~~ emissivity for low-
335 frequency channels ~~can be approximated by the pseudo-emissivity, because the interaction~~
336 ~~between the MW radiation and the atmosphere in the MW low-frequency channels is not~~
337 ~~significant~~, especially in cold and dry conditions. ~~For that reason, the 23 GHz pseudo-emissivity~~
338 ~~(pem₂₃) and the 31 GHz pseudo-emissivity (pem₃₁) have been used.~~ In Figure 3 (top panel) it is
339 possible to observe that there are sea ice classified observations characterized by the contemporary presence of
340 open water and sea ice above the bisector of the plane and in correspondence with low emissivity values. In the
341 center panel, where the color represents sea ice occurrences, it is evident the presence of ~~a~~ [one](#) cluster, in
342 correspondence with high pseudo-emissivity, with two “tails”: ~~the one~~ above ~~and below~~ the bisector, ~~the~~
343 ~~other below it~~. This behavior has been used to identify 3 different sea ice classes (New Sea Ice, Broken Sea Ice,
344 and Multilayer Sea Ice). ~~This algorithm is based on~~ using a Nearest [Neighbour/Neighbor](#) Method based
345 on a set of [reference](#) points that define the areas of interest for each sea ice class. In Figure 3 (bottom panel) a
346 classification representation is reported, where the markers represent the [reference](#) points ~~on which the~~
347 ~~Nearest Neighbor method is based~~. The [names/labels](#) of the classes have been chosen by analyzing
348 ~~the/their~~ physical properties ~~of the classes~~ and by comparing the estimated emissivity spectra with [those](#)
349 [reported in](#) previous [works/studies](#) ([Hewison & English, 1999](#), [Munchak et al, 2020](#)).

PESCA's upper working limits for T_{2m} and ~~atmospheric total precipitable water (TPW)~~ have been established to 280 K and 10 mm, respectively (see *Camplani et al, 2021* for details). Moreover, the land module does not work in the high elevation areas outside the polar regions (surface elevation > 2500 m for latitude < 67 ° N/S) because the ATMS low spatial resolution does not allow for depicting the small-scale snow-cover variability that characterizes the orographic regions. ~~Within these well-defined limits, the PESCA manages to optimally discriminate between sea ice, open water, snow-free land and snow-covered land.~~ An analysis carried out using the ATMS-CPR coincidence dataset highlights that the presence of cloud cover does not influence the overall PESCA performances (not shown). ~~Within these well-defined limits, the PESCA manages to optimally discriminate between sea ice, open water, snow-free land and snow-covered land.~~ The statistical scores (~~POD, FAR, HSS~~) of PESCA identification of sea ice and snow cover (using AutoSnow as the reference) are summarized in Table 1. In ~~the defined environmental conditions~~ particular, the Probability of Detection (POD), the False Alarm Ratio (FAR), and the Heidke Skill Score (HSS) are reported. POD, FAR, and HSS are defined by equations 2,3 and 4.

$$POD = \frac{h}{h+m}$$

(2)

$$FAR = \frac{f}{f+h}$$

(3)

$$HSS = \frac{2(h*cn - f*m)}{(h+m)*(m+cn) + (h+f)*(f+cn)}$$

(4)

where h represents the hits, f represents the false alarms, m represents the misses and cn represents the correct negatives. PESCA manages to optimally detect the presence of a frozen background (sea ice over the ocean, snow covered land over the continental part) at the time of the satellite overpass. It is important to underline that the ~~difference between variability of~~ the HSS values compared to POD and FAR is due to the different number of correct ~~negative observations, which has a strong influence on HSS values.~~ negatives. An analysis of the physical characteristics of the PESCA classes has been conducted by considering the mean T_{2m} , the geographical and seasonal distribution associated with each class. For what concerns the land class characteristics and properties, ~~classes, please~~ refer to *Camplani et al., 2021*. For what concerns sea ice, the New Sea Ice class, which is detected during the winter, at high latitudes, and for low temperatures, represents the sea ice that forms during the winter. The Broken Sea Ice class, which is predominant in the lower latitudes and whose occurrence increases during the ~~spring~~ Spring season, represents the co-presence of sea ice and water ~~typical of the intermediate seasons and in presence of melting phenomena.~~ The Multilayer Sea Ice class, which is detected only at the high latitudes, for very low temperatures, and ~~with a constant occurrence during~~ constantly e throughout the year, represents the ice pack typical of those regions ~~where extremely and extreme cold conditions allow its presence during the whole year.~~

3.1.2 PESCA emissivity spectra estimation

The emissivity spectra of each class have been estimated by applying the PESCA algorithm to the cloud-free (0% CPR cloud mask fraction, ~~i.e., clear sky~~) ATMS observations in the ATMS-CPR dataset satisfying PESCA working limits. The ATMS clear-sky TBs measured for each PESCA surface class have been used as input to an inverse radiative transfer model ~~(RTM) based on plane-parallel approximation (Ulaby & Long, 2014) and the Rosenkrantz (1998) gas absorption model.~~ The emissivity spectra have been estimated by calculating the mean and the standard deviation of the emissivity values for each class (excluding the values lower than the 10th percentile and higher than the 90th percentile). The emissivity spectra dependence on the ATMS viewing angle for polarized surfaces has been neglected because an analysis of such dependence in the ATMS-CPR coincidence dataset has shown that it is not significant ~~only~~ (emissivity difference smaller than 0.05 for larger viewing angles (tot for >40 up to 52.7 °). This is due to the fact that cross-track scanning radiometers measure a signal (off-nadir) which derives from a mixture between the two polarizations (e.g., quasi-vertical, QV, and quasi-horizontal, QH). As a consequence, although the emissivities of polarized surfaces, such as open water surfaces, are strongly influenced by the viewing angle, ~~for the cross-track scanning radiometers~~ the emissivity

398 variation is compensated by the effect of the mixture of the two polarizations (see also *Felde & Pickle, 1995,*
399 *Prigent et al, 2000, Mathew et al, 2008, Prigent et al, 2017*).

400 The estimated spectra are shown in Figure 4 and Figure 5 for ~~the land and~~ ocean ~~and land~~ classes, respectively;
401 ~~(the coast has also been considered as a separate class, however its spectrum is not shown in Figures 4-5).~~ It is
402 possible to observe that the classes are well-characterized from a radiometric point of view, showing distinct
403 behavior of the emissivity spectra (e.g., the mean values). However, all the classes present significant standard
404 deviations at high frequency, and some classes - such as the snow classes and the Broken Sea Ice class - present
405 a high value of standard deviation also at low frequency. ~~The coast observations have been also~~
406 ~~considered as a class, however its spectrum is not shown in Figures 4-5.~~

407 The ~~RMSE between simulated~~ clear-sky ~~TBs~~ ~~RTM simulations~~ based on the mean emissivity values
408 estimated for each class ~~and~~, ~~have been compared to~~ the coincident observed clear-sky TBs, ~~but the RMSE~~
409 ~~between simulated and observed clear-sky TBs appears~~ ~~appeared~~ to be too high to implement a robust signal
410 analysis (>10 K). For this reason, a refinement process for the emissivity spectra estimation based on machine
411 learning techniques has been developed downstream of the PESCA classification.

412 The refinement process has been based on a combination of an unsupervised classification technique (SOM) and
413 a supervised technique (LDA). The unsupervised classification identifies clusters characterized by the minimum
414 inner variability from a radiometric point of view. The supervised technique, instead, has the goal to identify the
415 previously obtained clusters, and the associated emissivity spectra, by using only input variables that are not
416 affected by the presence of clouds. The final emissivity spectra are estimated as the mean emissivity for each
417 frequency within each cluster identified by the supervised technique. Therefore, as first step, the emissivity ~~value~~
418 ~~set has~~ ~~spectra have~~ been clusterized in order to minimize the emissivity variability in each cluster by arranging
419 the retrieved emissivity values for six ATMS channels (23.8 GHz, 31.4 GHz, 50.3 GHz, 88.2 GHz, 165.5 GHz,
420 and 183.31±7 GHz) in a one-dimensional SOM architecture. Then, an LDA model has been trained using the
421 previously obtained clusters as reference and using the PESCA input parameters (**pem₂₃**, **pem₃₁**, **ratio** and **SI**),
422 some environmental parameters (**TPW**, **T_{2m}**, surface pressure - **P_{surf}**) and ancillary variables (latitude - **lat**, Julian
423 day - **jd**, altitude - **DEM**, the maximum solar height during the day - **H_{sun}**) as input. The use of the LDA is
424 necessary to associate an emissivity spectrum to all the observations which are classified by PESCA,
425 independently ~~from~~ the presence of clouds. It is worth noticing that the whole predictor set of the LDA has
426 resulted to be redundant; therefore, a subset of the predictors has been selected for each class. The accuracy of the
427 LDA classification is given by the ratio between the number of hits (observations where LDA identifies the
428 associated SOM class) and the total number of observations; it can be considered as an indicator of the
429 effectiveness of the LDA model in rebuilding the SOM results.

430 The evaluation of the refinement process is based on the comparison between the simulated clear-sky TBs and the
431 observed clear-sky TBs for each PESCA surface class. ~~An emissivity spectrum, (calculated as the mean~~
432 ~~of the emissivity values for each cluster), together with ECMWF temperature and water vapor~~
433 ~~profiles, is used as input in the RTM to simulate the clear-sky TBs.~~ For each PESCA surface class,
434 the number of clusters that simultaneously lowers the errors (RMSE) between the simulated and observed clear-
435 sky TBs at high frequency (without lowering the classification accuracy too much) is chosen.

436 In Table 2 the number of clusters, the predictors selected, the accuracy, RMSE and percentage normalized root
437 mean squared error (NRMSE%) (*Gareth et al, 2013*) estimated on the test dataset, are reported for the 165.5 GHz
438 channel. NRMSE% is defined by Equation 25.

$$439 \text{NRMSE}_{\%} = \left(\frac{\text{RMSE}}{\sigma} * 100 \right)$$

440 (25)

441 where σ represents the standard deviation of the measured clear-sky TBs dataset in each PESCA class. It can be
442 considered an indicator of the effectiveness of the refinement process.

443 For some classes, such as the Ocean class, the refinement process leads to ~~very~~ low RMSE values (~~≈ 2~~ (< 4 K)).
444 For other classes, such as Deep Dry Snow and Broken Sea Ice, RMSE remains > 5 K even with a high number
445 of clusters, although there is a significant reduction compared to the initial variance in each class (NRMSE% <
446 50). This is due to the variability of snow-covered background within each class; in the worst scenario, the
447 limited number of predictors are insufficient to infer the emissivity spectrum at high frequency. Overall, the

448 refinement process allows to obtain a general improvement of the accuracy of the [dynamic](#) emissivity estimation
449 for the PESCA classes; however, for some classes, the high-frequency channel uncertainty remains significant.
450 The emissivity spectra obtained by PESCA refinement are used as inputs of the RTM to obtain clear sky simulated
451 TBs (TB_{sim}) to be compared to the actual observations (TB_{obs}). The comparison between TB_{sim} with TB_{obs} allows
452 to highlight and interpret the MW signal in presence of snowfall.

453 In Figure 6, the snowfall signal is represented as a function of the SWP for the 165.5 GHz channel and for different
454 PESCA classes. The red line and shaded areas represent the mean values and standard deviations of the difference
455 between ~~the~~ TB_{obs} and ~~the~~ TB_{sim} ($\Delta TB_{obs-sim} = TB_{obs} - TB_{sim}$) for SWP bins calculated for observations where
456 $2CSP\ SWP > 0\ kg\ m^{-2}$. The blue lines represent the uncertainty due to surface emissivity variability for each
457 PESCA. They are centered on the estimated bias for each class (close to 0 K) and the dashed lines correspond to
458 the standard deviation of $\Delta TB_{obs-sim}$ in clear sky conditions. A clear scattering signal ($\Delta TB_{obs-sim} < 0$) is observed
459 over all the classes considered for intense snowfall events ($SWP > 1\ kg\ m^{-2}$). For lower SWP values, the signal is
460 more ambiguous and changes with the background surface. While over Land there is a clear scattering signal for
461 $SWP > 0.1\ kg\ m^{-2}$, over the Perennial Snow class a scattering signal can be observed only for $SWP > 0.5\ kg\ m^{-2}$
462 . For $SWP < 0.1\ kg\ m^{-2}$, the mean $\Delta TB_{obs-sim}$ for snowfall observations is less than its standard deviation in clear
463 sky. This is due mainly to the emissivity variability for each surface class, and to the error introduced by the use
464 of model-derived temperature and water vapor profiles in the RT simulations. However, while for the Land class
465 the mean $\Delta TB_{obs-sim} < 0\ K$ can be explained as a predominant scattering effect for all SWP values, for the Perennial
466 Snow class the mean $\Delta TB_{obs-sim} > 0\ K$ can be interpreted as a predominant emission signal with respect to the
467 radiatively cold background (Figure 5). The Thin Snow class shows an intermediate behavior: for $SWP < 0.1\ kg\ m^{-2}$
468 the red shaded area within the RMSE limits (blue lines) of the RT simulations denotes the difficulty in
469 interpreting the signal, while a clear scattering signal can be observed for $SWP > 0.3\ kg\ m^{-2}$. [For what concerns
470 ocean and new sea ice classes, a clear scattering signal is visible only for high SWP values \(\$> 1\ kg\ m^{-2}\$ \) while for
471 low SWP values a significant emission signal is observed. It is very likely that the emission effect observed over
472 ocean and sea ice is generated by supercooled cloud liquid water. The ubiquitous presence of supercooled water
473 layers in snowing clouds \(see \[Wang et al., 2013\]\(#\), \[Battaglia & Panegrossi, 2020\]\(#\)\), especially over oceans \(see
474 \[Battaglia & Delanoe, 2013\]\(#\)\), generates an emission effect which is particularly significant over radiatively cold
475 surfaces \(such as Perennial Snow, Ocean and New Sea Ice at high frequency, see Figure 4\), and can mask or
476 overcome the weak scattering signal generated by falling snow especially in light snowfall events. It is also
477 important to underline that the DARDAR product identifies mostly supercooled water layers at the cloud top
478 \(\[Rysman et al., 2018\]\(#\), \[Panegrossi et al., 2017\]\(#\)\), while it has been shown that the impact of supercooled water layers
479 embedded in the clouds can be very significant on the measured TBs at MW high frequency window channels
480 \(\[Battaglia & Panegrossi, 2020\]\(#\), \[Panegrossi et al., 2022\]\(#\)\).](#)

481 3.2 ANN Design for snowfall retrieval

482 The snowfall detection and estimation modules have been based on ANNs. Four ANNs have been developed: two
483 for the detection of SWP and SSR and two for the SWP and SSR estimate. The performance of more than 50
484 architectures have been tested, by varying the number of layers, the number of neurons for each layer, and the
485 activation functions. The final architecture, for all modules, is composed of four layers: an input layer with a
486 neurons number equal to the predictor number, and a hyperbolic tangent function as the activation function, a first
487 hidden layer (60 neurons), and hyperbolic tangent function, a second hidden layer (30 neurons), with a
488 ~~logarithmic tangent function~~ [sigmoid function \(for more information about the Neural Network
489 characteristics, see \[Sanò et al., 2015\]\(#\)\)](#). At the same time, several predictor sets have been tested combining in
490 different ways ATMS TB_{obs} , $\Delta TB_{obs-sim}$, PESCA surface class, ATMS angle of view, ancillary information
491 (surface elevation from a Digital Elevation Model), and model-derived environmental variables (T_{2m} , TPW, and
492 freezing level height). In Table 3 the statistical scores of the algorithm performance for the SSR detection module
493 obtained for different predictor sets are reported. It is possible to see that the best performance is obtained when
494 the predictor set is composed of ATMS TB_{obs} and $\Delta TB_{obs-sim}$, (besides PESCA surface flag, the pixel elevation
495 and the cosine of the viewing angle). In particular, it is [possible to observe an](#) ~~notable~~ [the](#) improvement of
496 the detection capabilities with respect to a predictor set composed of ATMS TB_{obs} and environmental parameters.
497 [On the other hand, the simultaneous use of both the \$\Delta TB_{obs-sim}\$ and the environmental parameters show scores
498 almost equal to that obtained by using only \$\Delta TB_{obs-sim}\$.](#) This indicates that the computation of the multi-channel
499 clear-sky TBs at the time of the overpass through the estimation of the [PESCAdynamic](#) surface class emissivity

spectra and its deviation from the measured TBs, ~~derived from the previous surface radiometric characterization obtained by PESCA~~, plays a fundamental role in snowfall retrieval. It provides essential information to the ANN to be able to exploit the subtle snowfall-related signal in ATMS measurements. This is the most innovative aspect of HANDEL-ATMS.

~~The~~ Based on these results, the final set of predictors for HANDEL-ATMS is composed by ~~the 16 ATMS 16ATMS channels~~ $T_{B_{obs}}$, ~~by~~ (1-9, 16-22, channels 10-15 have not been considered because their weighting function peaks above the tropopause), and the corresponding $\Delta T_{B_{obs-sim}}$ ~~set for the 16 ATMS channels~~, ~~from~~ the PESCA classification flag, the pixel elevation (obtained from a DEM) and the cosine of the view angle.

4. Results

4.1 HANDEL-ATMS Performances

In Table 4 the statistical scores of HANDEL-ATMS detection module performances are reported in terms of POD, FAR and HSS. It is possible to observe good detection capabilities both for SWP and SSR modules (POD > 0.8, FAR < 0.2).

In Figure 7 and in Figure 8 the dependence of HANDEL-ATMS snowfall detection statistical scores on TPW and on T_{2m} is reported. In both figures, it is possible to observe that the SWP detection capabilities improve (with an increase of POD and HSS and a decrease of FAR) with increasing humidity and temperature. This is due to the combined effect of a stronger scattering signal associated with more intense snowfall events - linked to moister and warmer environmental conditions - and to the lower transmissivity of the atmosphere which masks the background surface signal, reducing its impact and the uncertainties linked to its variability. On the other hand, colder and drier conditions are usually linked to background surface types characterized by high radiometric variability such as Perennial Snow and Winter Polar Snow classes, which cause uncertainty in emissivity estimation. It is possible to observe that in Figure 7 SSR detection capabilities show a maximum HSS value for TPW between 3 mm and 5 mm, and then there is a slight decrease due to the decrease of POD. A similar situation can be observed in Figure 8, where ~~HANDEL-ATMS SSR~~ the HSS reaches a maximum between 250 K and 275 K ~~and then decreases~~, and it is lower than for SWP. This is due to the fact that PMW measurements respond mostly to the snow in the atmospheric column and in moister/warmer conditions the presence of snow in the atmosphere is not always linked to surface snowfall. In both cases, it is worth noting that also considering very dry (TPW \approx 2 mm) or very cold ($T_{2m} \approx$ 240 K) conditions, HANDEL-ATMS shows good detection capabilities, in spite of the uncertainties linked to the modeling of the background surface and the weakness of the signal in such conditions. Moreover, ~~it is worth noticing that~~, also considering very low SWP and SSR values (SWP \approx 0.001 kg m⁻², SSR \approx 0.001 mm h⁻¹), HANDEL-ATMS manages to detect around 60 % of the snowfall events. Similar considerations can be done also for the different background surfaces. The detection capabilities are influenced both by the typical environmental conditions of each PESCA class and by the uncertainties linked to the emissivity estimation. In ~~Table 6~~ Figure 9 the statistical scores of the algorithm performance by considering each PESCA class for both the SWP and the SSR detection module are reported. It can be observed that, also considering specifically the classes associated to extremely dry and cold environmental conditions such as Perennial Snow or Winter Polar Snow (see Camplani et al, 2021), where the detection is more problematic ~~both for~~ due to the uncertainties linked to in the emissivity retrieval (see Table 2), ~~for the extremely dry and cold environmental conditions~~, and ~~for~~ to the low intensity of the snowfall events, ~~such as Perennial Snow or Winter Polar Snow~~, intensity, HANDEL-ATMS has good detection capabilities (POD and FAR values greater than 0.7 and less than 0.25, respectively, for both SWP and SSR). ~~These~~ On the other hand, for surface classes characterized by the highest emission estimation uncertainties, such as Deep Dry Snow, the statistical scores are coherent with the general scores and better than those obtained in presence of extremely dry/cold environmental conditions. So, it is possible to conclude that the extremely cold/dry environmental conditions - have more influence on the detection than the uncertainties on clear sky emissivity estimation. Generally, these results provide evidence that HANDEL-ATMS can be used to analyze snowfall occurrence in the polar regions.

The error statistics of the two estimation modules are reported in Table 5 in terms of bias, RMSE and the coefficient of determination R^2 , which is defined by Equation 36.

$$R^2 = 1 - \frac{RMSE^2}{std^2}$$

(36)

It is worth noticing that the biases are negligible for both modules while RMSE values are comparable to the light events recorded in the dataset. Moreover, as expected, RMSE and R^2 values are respectively higher and lower for the SSR module than for the SWP module; ~~this is due to the fact that the PMW signature is mainly related to the presence of snow in the atmosphere rather than to the surface snowfall rate.~~ In Figure 910 the density scatterplots between the SWP and SSR values retrieved by HANDEL-ATMS and the 2CSP corresponding values are reported. For both modules, an overestimation can be observed for very light snowfall ($SWP < 10^{-2} \text{ kg m}^{-2}$ and $SSR < 10^{-2} \text{ mm h}^{-1}$), while there is a very good agreement for higher SWP and SSR values. In order to relate these results to the environmental conditions, Figure 11 shows the dependence of HANDEL-ATMS snowfall estimation error statistics, as well of SWP and SSR, on TPW. The curves represent, for each 1-mm TPW bin, the mean 2-CSP SWP or SSR computed, the RMSE and the relative bias (the ratio between the bias and the SWP/SSR mean value for each bin). As expected, TPW and snowfall intensity are strongly correlated. An increase of the absolute RMSE can be observed as TPW increases, and it is larger than the SWP/SSR mean value for $TPW < 8 \text{ mm}$. A similar behavior can be observed by analyzing the dependence of HANDEL-ATMS snowfall estimation error statistics on T_{2m} (not shown). A very moderate overestimation is observed for $TPW < 8 \text{ mm}$ and for lower SWP and SSR values ($< 0.1 \text{ mm/h}$), with relative bias around 5%, (up to 8% only for extremely low TPW values and very low number of observations (see Figure 7)), while underestimation (relative bias up to -5%) is observed for higher TPW values and higher SWP and SSR values. Generally, light snowfall events are linked to the very cold/dry environmental conditions typical of high-latitude regions. So, the algorithm manages to estimate also the very light SWP and SSR typical of high latitudes but tends to slightly overestimate snowfall intensity in such conditions.

~~Generally~~From the analysis of Figure 7-11, it can be ~~observed~~concluded that, ~~although~~ HANDEL-ATMS ~~is able to detect~~has good detection capabilities (also for extremely light snowfall events,) but it ~~does not have the sensitivity to~~shows some limitations in correctly ~~estimate their~~estimating its intensity, ~~with slight overestimation of the very light snowfall typical of high latitudes.~~

4.2 A Case Study: Greenland-2016/04/24

The case study reported corresponds to the observation of a moderately light snowfall event over the central part of Greenland that occurred on 24 April 2016. ATMS overpass is between 14:51:23 U.T.CUTC. and 14:57:47 U.T.CUTC., while the CPR overpass is between 15:05:25 U.T.CUTC. and 15:11:45 U.T.CUTC., with a time difference of 14 minutes and 2 seconds. This event presents several characteristics typical of high latitudes, such as light snowfall rate, dry and cold atmospheric conditions, and presence of a frozen background surface, a typical case of interest for the application of HANDEL-ATMS.

In Figure 4012 PESCA classification is reported. The entire territory of Greenland, except for a narrow area on the southwestern coast, is identified as a snow-covered surface; PESCA identifies the Perennial Snow class in the central part of Greenland and along CloudSat track, and the Polar Winter Snow class near the northern shoreline. CloudSat overpasses the central part of the island, and CPR track is along the central part of the ATMS swath.

In Figure 4413 a synopsis of the event along the CPR track is reported: ~~the environmental parameters,~~ showing T_{2m} and TPW, the 2CSP SWP and SSR values, the cross-section of CPR reflectivity, with the DARDAR supercooled water information superimposed (in magenta). Moreover, the PESCA surface classification, and the TBs of the main ATMS high-frequency channels along the CloudSat track are ~~reported~~also shown. The event is characterized by dry conditions ($TPW < 5 \text{ mm}$) and T_{2m} below 273 K, except over the coast. CPR observes a cloud system linkedassociated to the snowfall event between 68°N and 76°N ; DARDAR detects the presence of a supercooled water layer at the cloud top between 68°N and 72°N and indicates the presence of supercooled droplets embedded in the deeper cloud associated to the more intense snowfall. According to the 2CSP detectsproduct, a light shallow snowfall eventsystem is found in the inner part of the island and a while deeper, more intense eventsnowfall, with a peak of intensity between 72°N and 76°N , is found near the shoreline. For what concerns the associated ATMS observations, an increase of the 88 GHz and 165 GHz TBs is observed in coincidencecorrespondence with the supercooled water layer; ~~on the other hand,~~ while only a slight decrease of 165.5 and 183.3+7 GHz TBs can be observed in coincidence with the snowfall intensity peak.

600 In figure 12 the maps of the TB_{obs} at 165.5 GHz (top panel) and the $\Delta TB_{obs-sim}$ at 165.5 GHz (bottom panel) are
601 reported. In the top panel, it is possible to observe that, despite the snowfall event, there is not a clear TB scattering
602 signal in the area where 2CSP detects snowfall (70°N–76°N, 40°W–70°W); instead a slight increase in the
603 TBs can be observed in the area where DARDAR detects the supercooled water layer ~~at the cloud top~~. The
604 ~~simulation map of the clear-sky TBs (TB_{sim})~~ $\Delta TB_{obs-sim}$ allows to observe an emission signal ($\Delta TB_{obs-sim} > 0$)
605 over the central part of the ATMS swath due to the combined effect of ~~the emission by the~~ supercooled liquid
606 water ~~emission (layers at the cloud top, as evidenced by DARDAR supercooled water layers)~~. (evidently
607 ~~exceeding the scattering signal of the weak~~ and ~~shallow snowfall~~), over a radiatively cold surface background.
608 Only near the shoreline, the TB_{obs} ~~is~~are slightly lower than the TB_{sim} ($\Delta TB_{obs-sim} < 0$) ~~due to the stronger~~
609 ~~scattering signal of the deeper snowfall system~~. In Figure 13 the results of the HANDEL-ATMS four modules
610 are reported. It is worth noting that both detection modules find snowfall in the central region of Greenland and
611 near the northern coast. The estimated ~~snowfall~~ intensity ~~of~~for this event is generally ~~light~~low (SWP < 0.1 kg m⁻²
612 and SSR < 0.1 mm h⁻¹) except over the western coast, where SWP reaches 0.5 kg m⁻² and SSR reaches 1 mm h⁻¹.
613 It is worth noticing that HANDEL-ATMS detects snowfall also where there is an emission signal ($\Delta TB_{obs-sim} >$
614 0) ~~and that discontinuities in snowfall retrievals are not observed in correspondence with surface class changes~~.
615 Finally, a comparison between the HANDEL-ATMS and the 2CSP is reported in Figure 14. ~~It is worth noting~~
616 ~~that there~~16. There is a substantial agreement on the snowfall detection of the two products. It can be observed
617 that HANDEL-ATMS tends to overestimate ~~both very light~~ SWP and SSR in presence of ~~very light~~
618 ~~snowfall~~shallow system (2CSP SWP < 0.05 kg m⁻² and SSR < 0.1 mm h⁻¹, between 68°N and 72°N),
619 consistently with what shown in Fig. 9; ~~on the other hand, Figure 10, while~~ there is a good agreement between
620 72°N and 76°N, where snowfall intensity increases.

621 The analysis of this case study demonstrates that the algorithm can interpret the ambiguity of the
622 emission/scattering signal ~~often~~ associated with snowfall ~~events at high latitudes (as described in Section 4.1)~~ and
623 ~~so~~ efficiently detect, and, ~~to a less extent~~, quantify snowfall even in extreme ~~cold and dry~~ conditions.

624 4.3 Comparison with SLALOM-CT

625 SLALOM-CT has been introduced in Section 1. It presents some similarities with HANDEL-ATMS: it is based
626 on an ANN approach and uses CPR-2CSP product as reference. On the other hand, substantial differences have
627 to be highlighted: SLALOM-CT was designed to operate on a global scale, while HANDEL-ATMS has been
628 developed specifically for the ~~extreme environmental~~ conditions typical of high latitudes. Moreover, the
629 predictor sets are different: in addition to TB observations, SLALOM-CT relies on several model derived
630 environmental parameters, while HANDEL-ATMS relies on differences between simulated clear-sky TBs ~~and~~
631 ~~observed TBs ($\Delta TB_{obs-sim}$)~~, ~~and therefore, based~~ on the ~~dynamic~~ estimation of the background surface
632 emissivity (i.e., at the time of the ~~satellite overpass~~), and ~~observed TBs ($\Delta TB_{obs-sim}$)~~, as described in Section 3.

633 In Table 7 a comparison between the statistical scores of the detection performances of the two algorithms is
634 reported for different environmental conditions. The comparison has been carried out considering the same
635 ~~observations elements~~ of the ATMS-CPR coincidence dataset. It can be observed that, ~~as in colder and~~
636 ~~drier conditions~~, the differences between the two algorithm performances increase: ~~HANDEL-ATMS~~
637 ~~shows~~ ~~as the environmental conditions become more extreme (i.e., lower T_{2m} and TPW), with consistently~~ better
638 snowfall detection capabilities ~~of HANDEL-ATMS~~ than SLALOM-CT. Considering the working limits of
639 HANDEL-ATMS, POD increases by 2 % and FAR decreases by 8 %; ~~however, if only~~%, while for
640 very cold/dry conditions ~~are considered~~ ($T_{2m} < 250$ K, TPW < 5 mm), POD increases by 7 % and FAR decreases
641 by 16 %; for extremely dry/cold conditions ($T_{2m} < 240$ K, TPW < 3 mm), typical of the inner part of Greenland
642 and Antarctica, POD increases by 18 % and FAR decreases by 16 %.

643 5 Conclusions and Future Perspectives

644 In this paper a new snowfall retrieval algorithm, the High Latitude sNow Detection and Estimation aLgorithm for
645 ATMS (HANDEL-ATMS), is described. The algorithm is based on machine learning techniques, ~~and it has~~
646 ~~been~~ trained ~~against with~~ CPR 2CSP snowfall ~~products. It has been developed product and it is designed~~
647 specifically for the ~~extreme cold and dry environmental~~ conditions typical of high latitude regions. The driving
648 and innovative principle in the algorithm development is the exploitation of the full range of ATMS channel
649 frequencies to characterize the ~~frozen~~ background surface radiative properties at the time of the overpass to be

650 able to better isolate and interpret the snowfall-related contribution to the measured multi-channel upwelling
651 radiation. [A similar approach has been used by Zhao & Weng, 2002; however, their application was limited to](#)
652 [non-scattering surfaces and was based on empirical relationships.](#) This approach is proven to be effective for
653 snowfall detection and quantification at high latitudes, particularly in presence of a frozen (snow-covered land or
654 sea ice) background [surface](#), also compared to other state-of-the art machine learning based methods.
655 HANDEL-ATMS can detect snowfall at high latitudes in good agreement with CPR. The estimation modules tend
656 to [slightly overestimate the intensity of light snowfall events \(SWP < 10⁻² kg m⁻²\), with mean relative bias < 5%](#)
657 [for SSR < 0.1 mm/h](#), but it shows good accuracy for more intense snowfall events (SWP > 10⁻² kg m⁻², SWP < 1
658 kg m⁻²). It is worth noting, however, that the uncertainty associated with the surface emissivity estimation in some
659 conditions affects the capabilities of HANDEL-ATMS to correctly interpret the snowfall signature. Such
660 uncertainty, ~~related to the difficulty in correctly modeling the intrinsic variability of snow cover~~
661 ~~surface emissivity~~, propagates in the [radiative transfer RTM](#) simulation of ~~the~~ clear-sky TBs used as input
662 in the algorithm. Despite these limitations, it is worth noticing that the development of an algorithm capable of
663 retrieving snowfall at high ~~latitudes~~ ~~conditions~~ with good accuracy is an important development in the climate
664 science field. The possibility to exploit ~~a big amount~~ [the high temporal sampling of data guaranteed by the](#)
665 ~~near-polar operational satellites carrying ATMS radiometers allows obtaining snowfall estimates~~
666 ~~characterized by a~~ [to achieve](#) full coverage of the polar ~~areas and a high temporal resolution~~ [regions](#).
667 Moreover, the future European MetOp Second Generation (MetOp-SG) mission, with the launch of the Sat-A
668 Microwave Sounder (MWS), with characteristics very similar to ATMS, will [soon](#) provide ~~another~~
669 ~~instrument~~ [additional coverage](#) to improve global snowfall monitoring. The HANDEL-ATMS methodology will
670 be ~~also~~ adapted to be able to exploit MWS measurements in the future. ~~The possibility to exploit a wide~~
671 ~~range of microwave channels allows obtaining a characterization of the background surface~~
672 ~~at the time of the overpass. This element is fundamental to obtain a characterization of the~~
673 ~~snowfall signature (especially for the extreme environmental conditions typical of high~~
674 ~~latitudes), and an accurate snowfall retrieval.~~ The capability to estimate snowfall ~~events with a~~ [at](#) high
675 temporal resolution is ancillary to the development of a ~~continuous~~ snowfall monitoring system ~~over~~ [for](#) the
676 high ~~latitude areas~~ [latitudes](#) and to ~~analyze~~ [the analysis of](#) the snowfall climatology in these areas. ~~This~~
677 ~~research could have important impacts, with possible applications~~ in climate change studies; ~~snowfall~~
678 ~~is predominant over rain in the high-latitude areas, and it has been proven that climate change~~
679 ~~has a strong impact on snowfall regime in these areas~~ [polar regions](#).
680 Future research ~~activities~~ will ~~tackle~~ [address](#) some open issues. The estimation of the surface emissivity and the
681 simulated clear-sky multi-channel TBs needs to be further improved, either by considering other predictor sets or
682 by using a different technique for the emissivity spectra ~~refinement process, or by using~~ [definition including](#)
683 ~~a~~ more advanced [radiative transfer models-RTM](#). Another important aspect is the quantification of the error
684 linked to the background [surface](#) emissivity estimation on the snowfall detection capabilities. This would be also
685 useful for the development of modules for mountainous areas, which have not been ~~analyzed in this~~
686 ~~study~~ ~~considered in the current version of the algorithm~~. Moreover, the effect on the algorithm snowfall detection
687 capabilities of the uncertainties linked to the model-derived environmental variables (e.g., temperature and water
688 vapor profile), which are used in the clear-sky TB simulations, should be investigated. The use of the ATMS water
689 vapor (183 GHz band) and temperature (50 GHz band) sounding channels to characterize the atmospheric
690 conditions at the time of the overpass in order to [complement or](#) avoid the use of model-derived data is another
691 subject of future research. Moreover, the ~~possible~~ development of a separate supercooled liquid water detection
692 module ~~could will be~~ ~~also~~ ~~be~~ evaluated, similarly to what is done in other PMW snowfall detection and estimation
693 algorithms (Rysman et al., 2018, Sanò et al., 2022). Such information can be exploited to improve snowfall
694 detection and estimation capabilities since the emission by the cloud droplets in dry conditions tends to mask the
695 snowfall scattering signal (see Panegrossi et al, 2017, Panegrossi et al, 2022), and adds larger uncertainties in the
696 CPR snowfall products (~~Battaglia & Panegrossi, 2021~~) ~~used as reference (Battaglia & Panegrossi, 2021)~~.
697 ~~Moreover, recent studies have highlighted that TBs correlate more strongly with lagged surface precipitation (with~~
698 ~~a time lag of 30-60 min for snowfall) than the simultaneous precipitation rate (see You et al, 2019). Therefore, an~~
699 ~~analysis based on a coincident dataset characterized by different time lags will be conducted. The results of this~~

700 [analysis will be compared with HANDEL-ATMS performances in order to identify a way to exploit this](#)
701 [information towards the improvement of SSR detection and estimation.](#) Finally, since the algorithm has been
702 developed only for specific environmental conditions typical [mostly](#) of high latitudes ~~(dry and cold~~
703 ~~atmosphere)~~ an integration with other approaches, such as SLALOM-CT, designed for global estimation of
704 snowfall, could be considered in the future to improve global snowfall monitoring based on ATMS and [on](#) future
705 cross-track scanning radiometers.

706 **Data availability**

707 ATMS data are provided by the NOAA CLASS facility www.avl.class.noaa.gov/ (last access 4 april 2023), CPR
708 data are distributed by the CloudSat data processing center <https://www.cloudsat.cira.colostate.edu/>
709 (last access 4 april 2023), DARDAR data are available from the ICARE FTP server of the University of Lille (ftp.icare.univ-
710 lille1.fr, last access 4 april 2023) and ECMWF operational forecasts are distributed by ECMWF through the
711 MARS facility via the ECGATE cluster. ~~AutoSnow~~AutoSnow data are provided by the NOAA Satellite and
712 Information Service https://satepsanone.nesdis.noaa.gov/northern_hemisphere_multisensor.html (last access 4
713 april 2023).

714 **Author Contribution**

715 Conceptualization, A.C., P.S., D.C.; methodology, A.C., P.S., D.C.; software, A.C.; validation, A.C.; formal
716 analysis, A.C.; investigation, A.C., P.S., D.C., G.P.; data curation, A.C. and D.C.; writing—original draft
717 preparation, A.C.; writing—review and editing, A.C., P.S., D.C., and G.P.; visualization, A.C.; supervision, G.P.;
718 project administration, G.P.; funding acquisition, G.P. All authors have read and agreed to the published version
719 of the manuscript.

720 **Competing Interests**

721 The authors declare no conflict of interest. The funders had no role in the design of the study; in the collection,
722 analyses, or interpretation of data; in the writing of the manuscript, or in the decision to publish the results.

723 **Acknowledgements**

724 This work was carried out under the RainCast study (ESA Contract No. 4000125959/18/NL/NA) and by the
725 EUMETSAT Satellite Application Facility for Operational Hydrology and Water management (H SAF) [Third and](#)
726 [Fourth](#) Continuous and Operations Phase (CDOP-[3](#) and CDOP-[4](#)). Andrea Camplani was supported by the Ph.D.
727 program in Infrastructures, Transport Systems and Geomatics at the Department of Civil, Constructional, and
728 Environmental Engineering at Sapienza University of Rome. The authors would like to thank EUMETSAT and
729 the NASA Precipitation Measurement Mission (PMM) Research Program for supporting scientific collaborations
730 between H SAF and GPM, and the PMM Science Team. The authors wish to express their sincere gratitude to Joe
731 Turk (NASA JPL) and Alessandro Battaglia [who](#) are warmly acknowledged for useful interactions and discussions
732 during the algorithm development and validation, and to Mattia Crespi for the scientific support to Andrea
733 Camplani during the Ph.D. program.

734 **References**

- 735 Battaglia, A., & Delanoë, J.: Synergies and complementarities of CloudSat-CALIPSO snow observations. *Journal*
736 *of Geophysical Research: Atmospheres*, 118(2), 721-731. <https://doi.org/10.1029/2012JD018092>, 2013.
- 737 Battaglia, A., & Panegrossi, G.: What can we learn from the CloudSat radiometric mode observations of snowfall
738 over the ice-free ocean? *Remote Sensing*, 12(20), 3285, <https://doi.org/10.3390/rs12203285>, 2020.
- 739 Behrangi, A., Christensen, M., Richardson, M., Lebsock, M., Stephens, G., Huffman, G. J., Bolvin, D., Adler, R.
740 F., Gardner, A., Lambrigsten, B., & Fetzer, E.: Status of high-latitude precipitation estimates from observations
741 and reanalyses. *Journal of Geophysical Research: Atmospheres*, 121(9), 4468-4486,
742 <https://doi.org/10.1002/2015JD024546>, 2016.
- 743 Bintanja, R., Selten, F.: Future increases in Arctic precipitation linked to local evaporation and sea-ice retreat.
744 *Nature* 509, 479–482, <https://doi.org/10.1038/nature13259>, 2014.
- 745 Camplani, A., Casella, D., Sanò, P., & Panegrossi, G.: The Passive microwave Empirical cold Surface
746 Classification Algorithm (PESCA): Application to GMI and ATMS. *Journal of Hydrometeorology*, 22(7), 1727-
747 1744, <https://doi.org/10.1175/JHM-D-20-0260.1>, 2021.
- 748 Casella, D., Panegrossi, G., Sanò, P., Marra, A. C., Dietrich, S., Johnson, B. T., & Kulie, M. S.: Evaluation of the
749 GPM-DPR snowfall detection capability: Comparison with CloudSat-CPR. *Atmospheric Research*, 197, 64-75,
750 <https://doi.org/10.1016/j.atmosres.2017.06.018>, 2017.

752 Ceccaldi, M., Delanoë, J., Hogan, R. J., Pounder, N. L., Protat, A., & Pelon, J.: From CloudSat-CALIPSO to
753 EarthCare: Evolution of the DARDAR cloud classification and its comparison to airborne radar-lidar
754 observations. *Journal of Geophysical Research: Atmospheres*, 118(14), 7962-7981,
755 <https://doi.org/10.1002/jgrd.50579>, 2013.

756 DARDAR- retrieve cloud properties by combining the CloudSat radar and the CALIPSO lidar measurements.
757 CNS-CNRS-Universiteé de Lille., <https://www.icare.univ-lille.fr/dardar/>, last access: 4 April 2023.

758 Clifford, D.: Global estimates of snow water equivalent from passive microwave instruments: history, challenges
759 and future developments. *International Journal of Remote Sensing*, 31(14), 3707-3726,
760 <https://doi.org/10.1080/01431161.2010.483482>, 2010.

761 Comiso, J. C.: Sea ice effective microwave emissivities from satellite passive microwave and infrared
762 observations. *Journal of Geophysical Research: Oceans*, 88(C12), 7686-7704.
763 <https://doi.org/10.1029/JC088iC12p07686>, 1983

764 Cordisco, E., Prigent, C., & Aires, F.: Snow characterization at a global scale with passive microwave satellite
765 observations. *Journal of Geophysical Research: Atmospheres*, 111(D19), <https://doi.org/10.1029/2005JD006773>,
766 2006.

767 Fausett, L. V., Fundamentals of neural networks: architectures, algorithms and applications, Pearson Education
768 India, ISBN-13: 978-0133341867, 1994.

769 Felde, G. W., & Pickle, J. D.: Retrieval of 91 and 150 GHz Earth surface emissivities. *Journal of Geophysical*
770 *Research: Atmospheres*, 100(D10), 20855-20866, <https://doi.org/10.1029/95JD02221>, 1995.

771 Gareth, J., Daniela, W., Trevor, H., & Robert, T.: An introduction to statistical learning: with applications in R.
772 Springer, ISBN-13:978-1461471370 , 2013.

773 Grody, N. C., & Basist, A. N.: Global identification of snowcover using SSM/I measurements. *IEEE Transactions*
774 *on geoscience and remote sensing*, 34(1), 237-249, DOI: 10.1109/36.481908, 1996.

775 Hastie, T., Tibshirani, R., Friedman, J. H., & Friedman, J. H.: *The elements of statistical learning: data mining,*
776 *inference, and prediction* (Vol. 2, pp. 1-758). New York: springer, DOI: 10.1007/b94608, 2009.

777 Kidd, C., & Huffman, G.: Global precipitation measurement. *Meteorological Applications*, 18(3), 334-353,
778 <https://doi.org/10.1002/met.284>, 2011.

779 Hewison, T. J., & English, S. J.: Airborne retrievals of snow and ice surface emissivity at millimeter wavelengths.
780 *IEEE Transactions on Geoscience and Remote Sensing*, 37(4), 1871-1879, DOI: 10.1109/36.774700, 1999.

781 Kim, M. J., Weinman, J. A., Olson, W. S., Chang, D. E., Skofronick-Jackson, G., & Wang, J. R.: A physical
782 model to estimate snowfall over land using AMSU-B observations. *Journal of Geophysical Research:*
783 *Atmospheres*, 113(D9), <https://doi.org/10.1029/2007JD008589>, 2008.

784 Kohonen, T.: *Self-organization and associative memory* (Vol. 8). Springer Science & Business Media,
785 DOI:10.1007/978-3-642-88163-3, 2012.

786 Kongoli, C., Pellegrino, P., Ferraro, R. R., Grody, N. C., & Meng, H.: A new snowfall detection algorithm over
787 land using measurements from the Advanced Microwave Sounding Unit (AMSU). *Geophysical Research Letters*,
788 30(14). <https://doi.org/10.1029/2003GL017177>, 2003.

789 Kongoli, C., Meng, H., Dong, J., & Ferraro, R.: A snowfall detection algorithm over land utilizing high-frequency
790 passive microwave measurements—Application to ATMS. *Journal of Geophysical Research: Atmospheres*,
791 120(5), 1918-1932, <https://doi.org/10.1002/2014JD022427>, 2015.

792 Kongoli, C., Meng, H., Dong, J., & Ferraro, R.: A hybrid snowfall detection method from satellite passive
793 microwave measurements and global forecast weather models. *Quarterly Journal of the Royal Meteorological*
794 *Society*, 144, 120-132. <https://doi.org/10.1002/qj.3270>, 2018.

795 Kulie, M. S., Bennartz, R., Greenwald, T. J., Chen, Y., & Weng, F.: Uncertainties in microwave properties of
796 frozen precipitation: Implications for remote sensing and data assimilation. *Journal of the Atmospheric Sciences*,
797 67(11), 3471-3487. <https://doi.org/10.1175/2010JAS3520.1>, 2010.

798 Kulie, M. S., Milani, L., Wood, N. B., Tushaus, S. A., Bennartz, R., & L'Ecuyer, T. S.: A shallow cumuliform
799 snowfall census using spaceborne radar. *Journal of Hydrometeorology*, 17(4), 1261-1279.
800 <https://doi.org/10.1175/JHM-D-15-0123.1>, 2016.

801 Levizzani, V., Laviola, S., & Cattani, E.: Detection and measurement of snowfall from space. *Remote Sensing*,
802 3(1), 145-166, <https://doi.org/10.3390/rs3010145>, 2011.

803 Liu, Y., Key, J. R., Liu, Z., Wang, X., & Vavrus, S. J.: A cloudier Arctic expected with diminishing sea ice.
804 *Geophysical Research Letters*, 39(5). <https://doi.org/10.1029/2012GL051251>, 2012.

805 Liu, J., Curry, J. A., Wang, H., Song, M., & Horton, R. M.: Impact of declining Arctic sea ice on winter snowfall.
806 *Proceedings of the National Academy of Sciences*, 109(11), 4074-4079. <https://doi.org/10.1073/pnas.1114910109>,
807 2012.

808 Liu, G., & Seo, E. K.: Detecting snowfall over land by satellite high-frequency microwave observations: The lack
809 of scattering signature and a statistical approach. *Journal of geophysical research: atmospheres*, 118(3), 1376-
810 1387, <https://doi.org/10.1002/jgrd.50172>, 2013.

811 Mathew, N., Heygster, G., Melsheimer, C., & Kaleschke, L.: Surface emissivity of Arctic sea ice at AMSU
812 window frequencies. *IEEE transactions on geoscience and remote sensing*, 46(8), 2298-2306,
813 DOI: [10.1109/TGRS.2008.916630](https://doi.org/10.1109/TGRS.2008.916630), 2008.

814 Mätzler, C., & Hüppi, R.: Review of signature studies for microwave remote sensing of snowpacks. *Advances in*
815 *Space Research*, 9(1), 253-265, [https://doi.org/10.1016/0273-1177\(89\)90493-6](https://doi.org/10.1016/0273-1177(89)90493-6), 1989.

816 Meng, H., Dong, J., Ferraro, R., Yan, B., Zhao, L., Kongoli, C., Wang, N., & Zavadsky, B.: A 1DVAR-based
817 snowfall rate retrieval algorithm for passive microwave radiometers. *Journal of Geophysical Research:*
818 *Atmospheres*, 122(12), 6520-6540. <https://doi.org/10.1002/2016JD026325>, 2017.

819 Milani, L., Kulie, M. S., Casella, D., Dietrich, S., L'Ecuyer, T. S., Panegrossi, G., Porcù, F., Sanò, P., & Wood,
820 N. B.: CloudSat snowfall estimates over Antarctica and the Southern Ocean: An assessment of independent
821 retrieval methodologies and multi-year snowfall analysis. *Atmospheric research*, 213, 121-135,
822 <https://doi.org/10.1016/j.atmosres.2018.05.015>, 2018.

823 Milani, L., & Wood, N. B.: Biases in cloudsat falling snow estimates resulting from daylight-only operations.
824 *Remote Sensing*, 13(11), 2041, <https://doi.org/10.3390/rs13112041>, 2021.

825 Mroz, K., Montopoli, M., Battaglia, A., Panegrossi, G., Kirstetter, P., & Baldini, L.: Cross validation of active
826 and passive microwave snowfall products over the continental United States. *Journal of Hydrometeorology*, 22(5),
827 1297-1315. <https://doi.org/10.1175/JHM-D-20-0222.1>, 2021.

828 Munchak, S. J., Ringerud, S., Brucker, L., You, Y., de Gelis, I., & Prigent, C.: An active-passive microwave land
829 surface database from GPM. *IEEE Transactions on Geoscience and Remote Sensing*, 58(9), 6224-6242, DOI:
830 10.1109/TGRS.2020.2975477, 2020.

831 Noh, Y. J., Liu, G., Jones, A. S., & Vonder Haar, T. H.: Toward snowfall retrieval over land by combining satellite
832 and in situ measurements. *Journal of Geophysical Research: Atmospheres*, 114(D24),
833 <https://doi.org/10.1029/2009JD012307>, 2009.

834 Panegrossi, G., Rysman, J. F., Casella, D., Marra, A. C., Sanò, P., & Kulie, M. S.: CloudSat-based assessment of
835 GPM Microwave Imager snowfall observation capabilities. *Remote Sensing*, 9(12), 1263,
836 <https://doi.org/10.3390/rs9121263>, 2017.

837 Panegrossi, G., Casella, D., Sanò, P., Camplani, A., & Battaglia, A.: Recent advances and challenges in satellite-
838 based snowfall detection and estimation. *Precipitation Science*, 333-376, <https://doi.org/10.1016/B978-0-12-822973-6.00015-9>, 2022.

840 Partain, P.: CloudSat ECMWF-AUX Auxiliary Data Product Process Description and Interface Control
841 Document, Product Version P1_R05, NASA JPL CloudSat project document revision 0, pp. 16, Available from:
842 [https://www.cloudsat.cira.colostate.edu/cloudsat-static/info/dl/ecmwf-aux/ECMWF-
843 AUX.PDICD.P1_R05.rev0.pdf](https://www.cloudsat.cira.colostate.edu/cloudsat-static/info/dl/ecmwf-aux/ECMWF-AUX.PDICD.P1_R05.rev0.pdf), 2022

844 Prigent, C., Wigneron, J. P., Rossow, W. B., & Pardo-Carrion, J. R.: Frequency and angular variations of land
845 surface microwave emissivities: Can we estimate SSM/T and AMSU emissivities from SSM/I emissivities?. *IEEE*
846 *transactions on geoscience and remote sensing*, 38(5), 2373-2386, DOI:10.1109/36.868893, 2000.

847 Prigent, C., Aires, F., Rossow, W., & Matthews, E.: Joint characterization of vegetation by satellite observations
848 from visible to microwave wavelengths: A sensitivity analysis. *Journal of Geophysical Research: Atmospheres*,
849 106(D18), 20665-20685, <https://doi.org/10.1029/2000JD900801>, 2001.

850 Prigent, C., Jaumouille, E., Chevallier, F., & Aires, F.: A parameterization of the microwave land surface
851 emissivity between 19 and 100 GHz, anchored to satellite-derived estimates. *IEEE Transactions on Geoscience*
852 *and Remote Sensing*, 46(2), 344-352, DOI: 10.1109/TGRS.2007.908881, 2008.

853 Prigent, C., Aires, F., Wang, D., Fox, S., & Harlow, C.: Sea-surface emissivity parametrization from microwaves
854 to millimetre waves. *Quarterly Journal of the Royal Meteorological Society*, 143(702), 596-605.
855 <https://doi.org/10.1002/qj.2953>, 2017.

856 Rahimi, R., Ebtehaj, A., Panegrossi, G., Milani, L., Ringerud, S. E., & Turk, F. J., Vulnerability of Passive
857 Microwave Snowfall Retrievals to Physical Properties of Snowpack: A Perspective From Dense Media Radiative
858 Transfer Theory. *IEEE Transactions on Geoscience and Remote Sensing*, 60, 1-13,
859 <https://doi.org/10.3390/rs11192200>, 2017.

860 Romanov, P.: Global multisensor automated satellite-based snow and ice mapping system (GMASI) for
861 cryosphere monitoring. *Remote Sensing of Environment*, 196, 42-55, <https://doi.org/10.1016/j.rse.2017.04.023>,
862 2017.

863 [Rosenkranz, P. W.. Water vapor microwave continuum absorption: A comparison of measurements and models. *Radio Science*, 33\(4\), 919-928. <https://doi.org/10.1029/98RS01182>, 1998.](https://doi.org/10.1029/98RS01182)

864 Rysman, J. F., Panegrossi, G., Sanò, P., Marra, A. C., Dietrich, S., Milani, L., & Kulie, M. S.: SLALOM: An all-
865 surface snow water path retrieval algorithm for the GPM Microwave Imager. *Remote Sensing*, 10(8), 1278,
866 <https://doi.org/10.3390/rs10081278>, 2018.

867 Rysman, J. F., Panegrossi, G., Sano, P., Marra, A. C., Dietrich, S., Milani, L., Kulie, M. S., Casella, D., Camplani,
868 A., Claud, C., & Edel, L.: Retrieving surface snowfall with the GPM Microwave Imager: A new module for the
869 SLALOM algorithm. *Geophysical Research Letters*, 46(22), 13593-13601,
870 <https://doi.org/10.1029/2019GL084576>, 2019.

871 Sanò, P., Casella, D., Camplani, A., D'Adderio, L. P., & Panegrossi, G., A Machine Learning Snowfall Retrieval
872 Algorithm for ATMS. *Remote Sensing*, 14(6), 1467, <https://doi.org/10.3390/rs14061467>, 2022.

873 Sanò, P., Panegrossi, G., Casella, D., Di Paola, F., Milani, L., Mugnai, A., Petracca, M., & Dietrich, S. (2015).
874 The Passive microwave Neural network Precipitation Retrieval (PNPR) algorithm for AMSU/MHS observations:
875 description and application to European case studies. *Atmospheric Measurement Techniques*, 8(2), 837-857,
876 <https://doi.org/10.5194/amt-8-837-2015>, 2015.

877 Skofronick-Jackson, G. M., Kim, M. J., Weinman, J. A., & Chang, D. E. (2004). A physical model to determine
878 snowfall over land by microwave radiometry. *IEEE Transactions on Geoscience and Remote Sensing*, 42(5),
879 1047-1058, DOI:10.1109/TGRS.2004.825585, 2004.

880 Skofronick-Jackson, G., Hudak, D., Petersen, W., Nesbitt, S. W., Chandrasekar, V., Durden, S., Kristin, J. G.,
881 Huang, G., Joe, P., Kollias, P., Reed, K., A., Schwaller, M., R., Stewart, R., Tanelli, S., Tokay, A., Wang, J., R.,
882 & Wolde, M.: Global precipitation measurement cold season precipitation experiment (GCPEX): For
883 measurement's sake, let it snow. *Bulletin of the American Meteorological Society*, 96(10), 1719-1741,
884 <https://doi.org/10.1175/BAMS-D-13-00262.1>, 2015.

885 Stephens, G. L., Vane, D. G., Tanelli, S., Im, E., Durden, S., Rokey, M., Reinke, D., Partain, P., Mace, G. G.,
886 Austin, R., L'Ecuyer, T., Haynes, J., Lebsock, M., Suzuki, K., Waliser, D., Wu, D., Kay, J., Gettelman, A., Zhien
887 Wang, Z., & Marchand, R.: CloudSat mission: Performance and early science after the first year of operation.
888 *Journal of Geophysical Research: Atmospheres*, 113(D8), <https://doi.org/10.1029/2008JD009982>, 2008.

889 Takbiri, Z., Ebtehaj, A., Foufloula-Georgiou, E., Kirstetter, P. E., & Turk, F. J.: A prognostic nested k-nearest
890 approach for microwave precipitation phase detection over snow cover. *Journal of hydrometeorology*, 20(2), 251-
891 274, <https://doi.org/10.1175/JHM-D-18-0021.1>, 2019.

892 Turk, F. J., Ringerud, S. E., Camplani, A., Casella, D., Chase, R. J., Ebtehaj, A., Gong, J., Kulie, M., Liu, G.,
893 Milani, L., Panegrossi, G., Padullés, R., Rysman, J. F., Sanò, P., Vahedizade, S., & Wood, N. B.: Applications of
894 a CloudSat-TRMM and CloudSat-GPM satellite coincidence dataset. *Remote Sensing*, 13(12), 2264,
895 <https://doi.org/10.3390/rs13122264>, 2021a.

896 Turk, F. J., Ringerud, S. E., You, Y., Camplani, A., Casella, D., Panegrossi, G., Sanò, P., Ebtehaj, A., Guilloteau,
897 C., Utsumi, N., Prigent, C., & Peters-Lidard, C.: Adapting passive microwave-based precipitation algorithms to
898 variable microwave land surface emissivity to improve precipitation estimation from the GPM constellation.
899 *Journal of Hydrometeorology*, 22(7), 1755-1781, <https://doi.org/10.1175/JHM-D-20-0296.1>, 2021.

900 Ulaby, F., & Long, D., Microwave radar and radiometric remote sensing, 1st Edition, the Univ. of Michigan Press,
901 ISBN: 978-0-472-11935-6, 2014.

902 Vihma, T., Screen, J., Tjernström, M., Newton, B., Zhang, X., Popova, V., Deser, C., Holland, M., & Prowse, T.:
903 The atmospheric role in the Arctic water cycle: A review on processes, past and future changes, and their impacts.
904

905 *Journal of Geophysical Research: Biogeosciences*, 121(3), 586-620, <https://doi.org/10.1002/2015JG003132>,
906 2016.
907 [Wang, Y., Liu, G., Seo, E. K., & Fu, Y.: Liquid water in snowing clouds: Implications for satellite remote sensing](https://doi.org/10.1016/j.atmosres.2012.06.008)
908 [of snowfall. *Atmospheric research*, 131, 60-72, https://doi.org/10.1016/j.atmosres.2012.06.008,2013.](https://doi.org/10.1016/j.atmosres.2012.06.008)
909 Weng, F., Zou, X., Wang, X., Yang, S., & Goldberg, M. D.: Introduction to Suomi national polar-orbiting
910 partnership advanced technology microwave sounder for numerical weather prediction and tropical cyclone
911 applications. *Journal of geophysical research: atmospheres*, 117(D19), <https://doi.org/10.1029/2012JD018144>,
912 2012.
913 Wood, N. B. and T. S. L'Ecuyer: Level 2C Snow Profile Process Description and Interface Control Document,
914 Product Version P1 R05. NASA JPL CloudSat project document revision 0., 26 pp, Available from
915 [https://www.cloudsat.cira.colostate.edu/cloudsat-static/info/dl/2c-snow-profile/2C-SNOW-](https://www.cloudsat.cira.colostate.edu/cloudsat-static/info/dl/2c-snow-profile/2C-SNOW-PROFILE_PDICD.P1_R05.rev0_.pdf)
916 [PROFILE_PDICD.P1_R05.rev0_.pdf](https://www.cloudsat.cira.colostate.edu/cloudsat-static/info/dl/2c-snow-profile/2C-SNOW-PROFILE_PDICD.P1_R05.rev0_.pdf), 2018.
917 You, Y., Meng, H., Dong, J., Fan, Y., Ferraro, R. R., Gu, G., & Wang, L.: A Snowfall Detection Algorithm for
918 ATMS Over Ocean, Sea Ice, and Coast. *IEEE Journal of Selected Topics in Applied Earth Observations and*
919 *Remote Sensing*, 15, 1411-1420, DOI:[10.1109/JSTARS.2022.3140768](https://doi.org/10.1109/JSTARS.2022.3140768), 2022.
920

921 [You, Y., Meng, H., Dong, J., & Rudlosky, S.: Time-lag correlation between passive microwave measurements](#)
922 [and surface precipitation and its impact on precipitation retrieval evaluation. *Geophysical Research Letters*,](#)
923 [46\(14\), 8415-8423, doi: 10.1029/2019GL083426, 2019.](#)

924 [Zhao, L., & Weng, F.: Retrieval of ice cloud parameters using the Advanced Microwave Sounding Unit. *Journal*](#)
925 [of Applied Meteorology and Climatology, 41\(4\), 384-395, https://www.jstor.org/stable/26184983, 2002.](#)

926

927

928

929

930

931

932

933

934

935

936

937

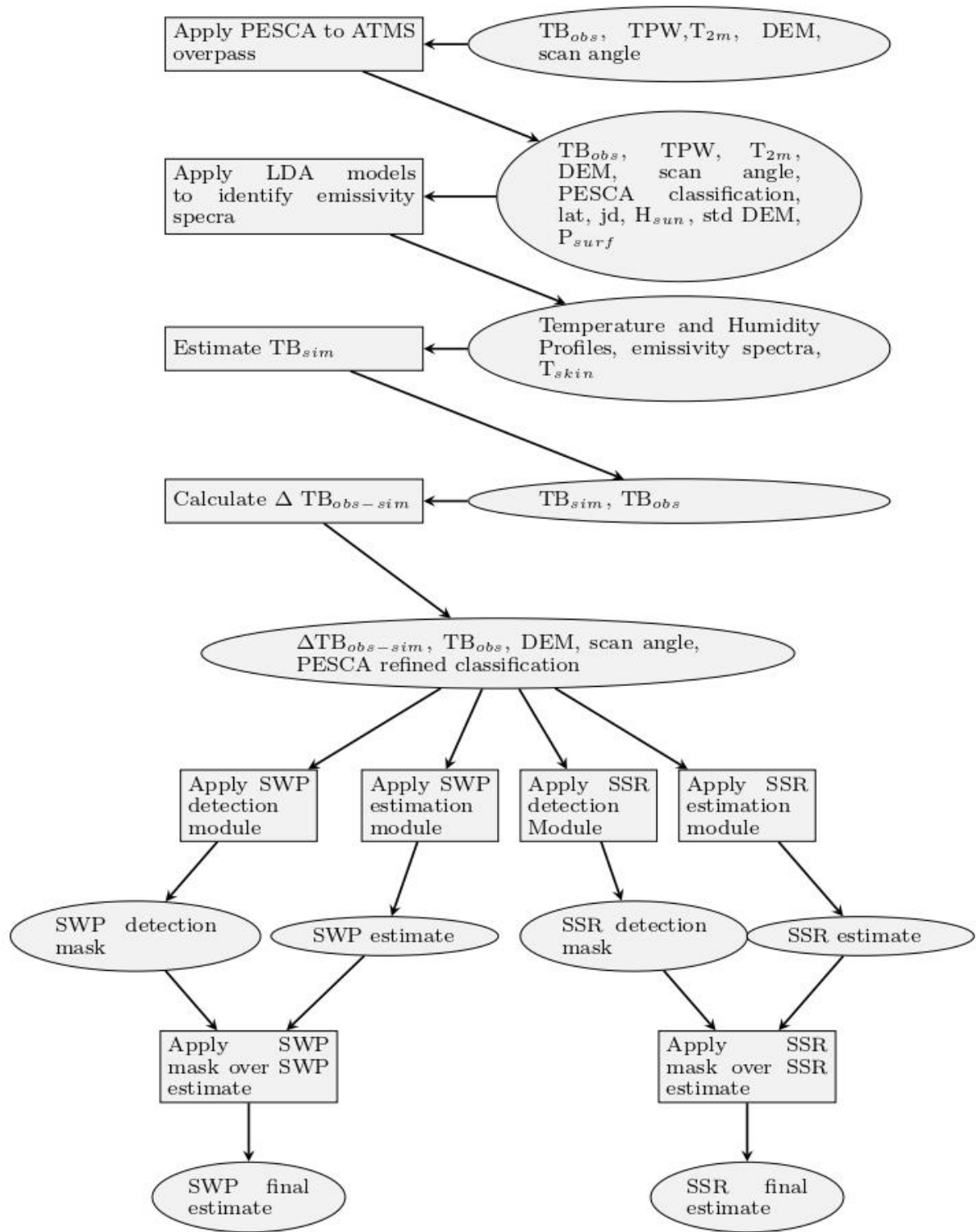
938

939

940

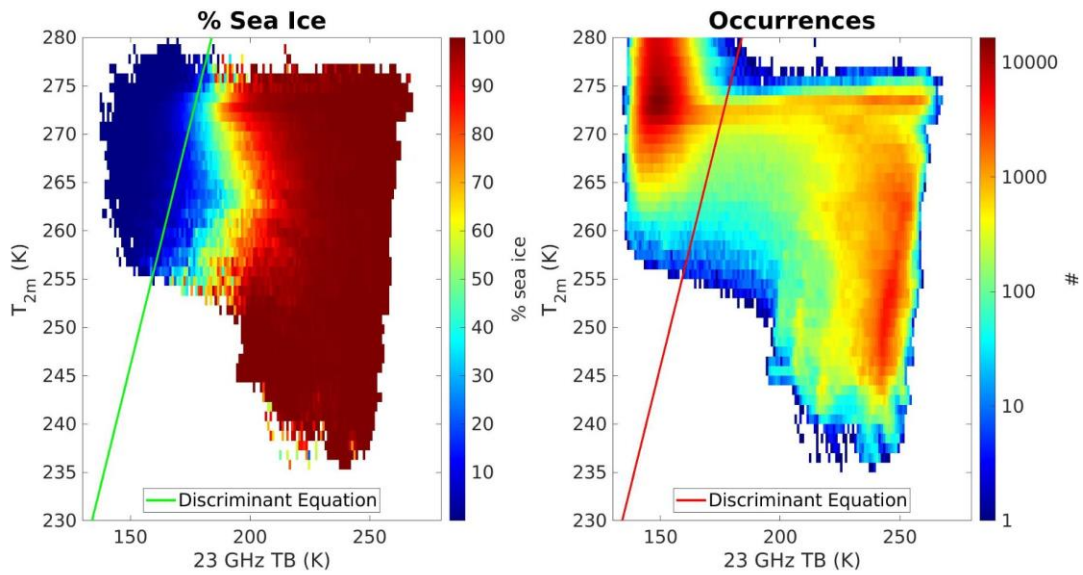
941 **Figures**

942



943
944
945

Figure 1: HANDEL-ATMS workflow diagram (please, refer to the text for details)



946
947
948
949
950

Figure 2: Sea Ice Detection: detection representation on a 23 TB- T_{2m} Plane. The color represents the mean AutoSnow sea ice percentage within each bin (left) and the observation occurrence (right). The green (left) and red (right) lines represent the discriminant Equation (Equation 1) between sea ice and ocean.

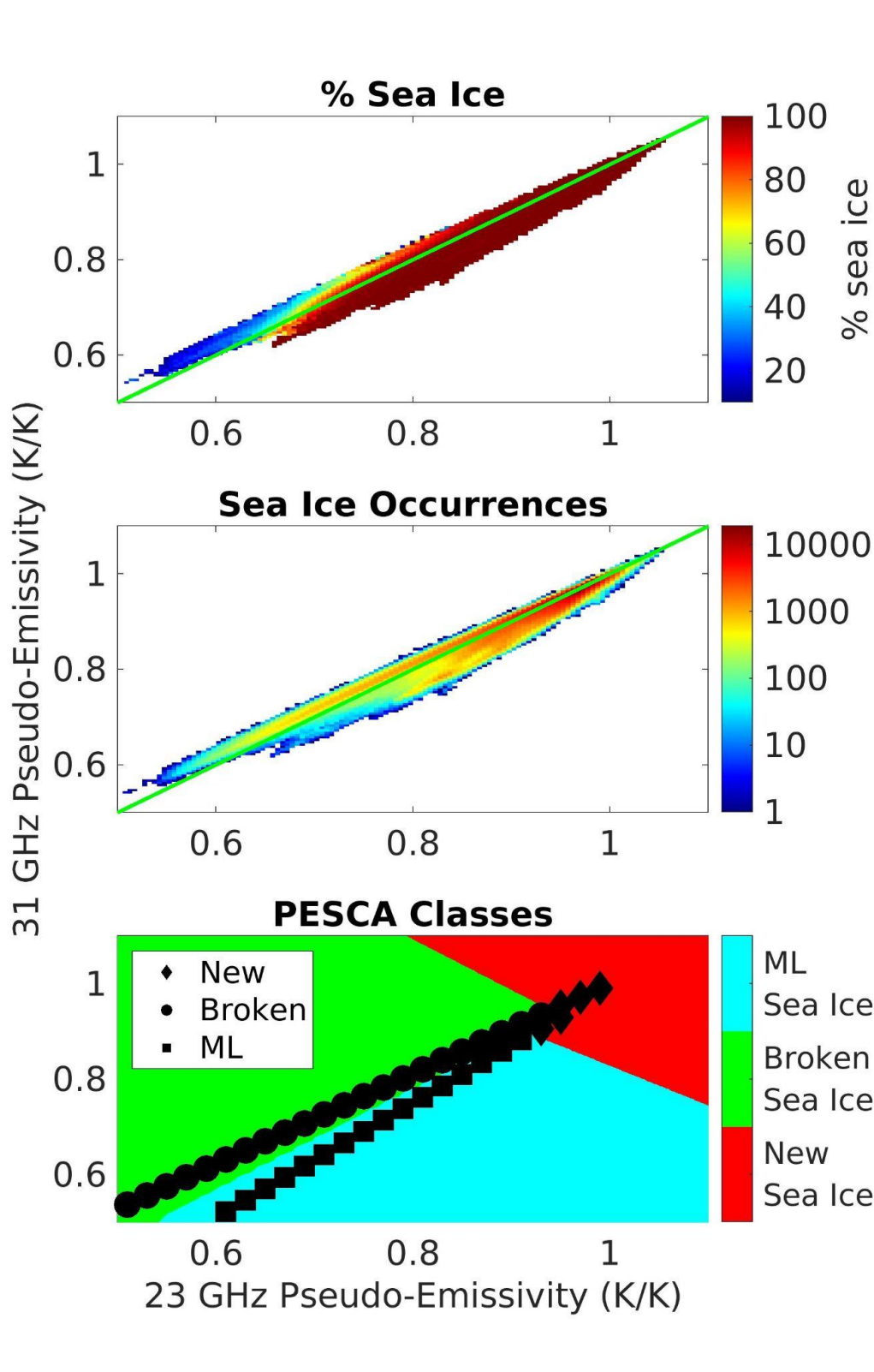
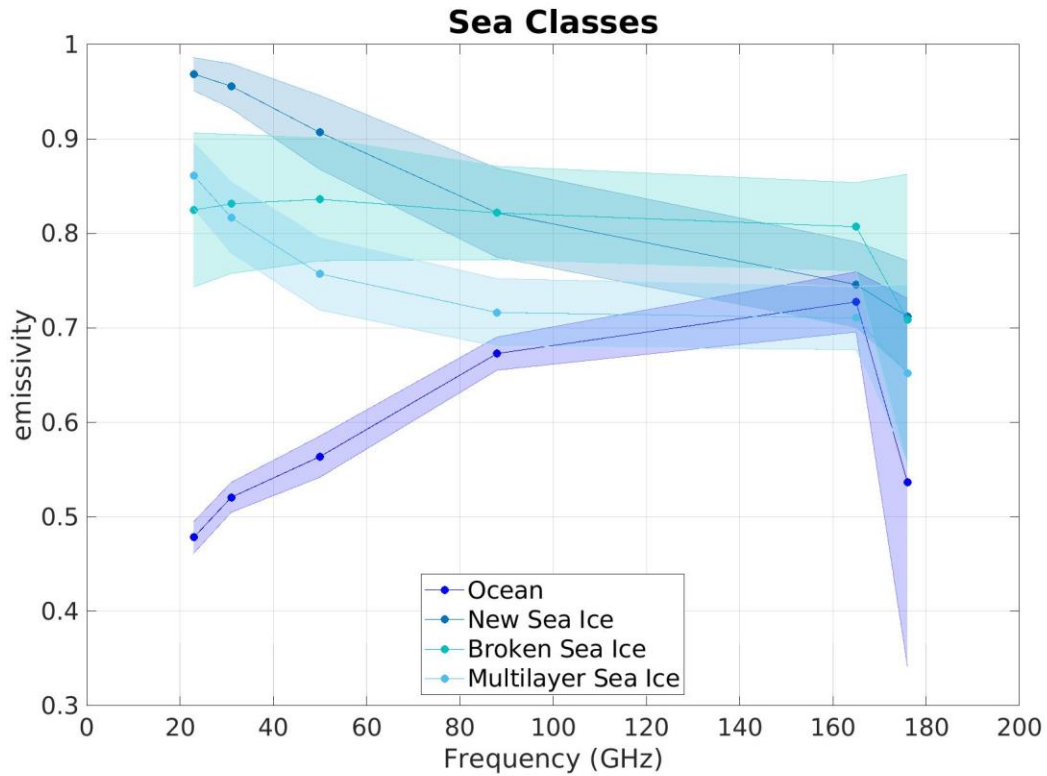
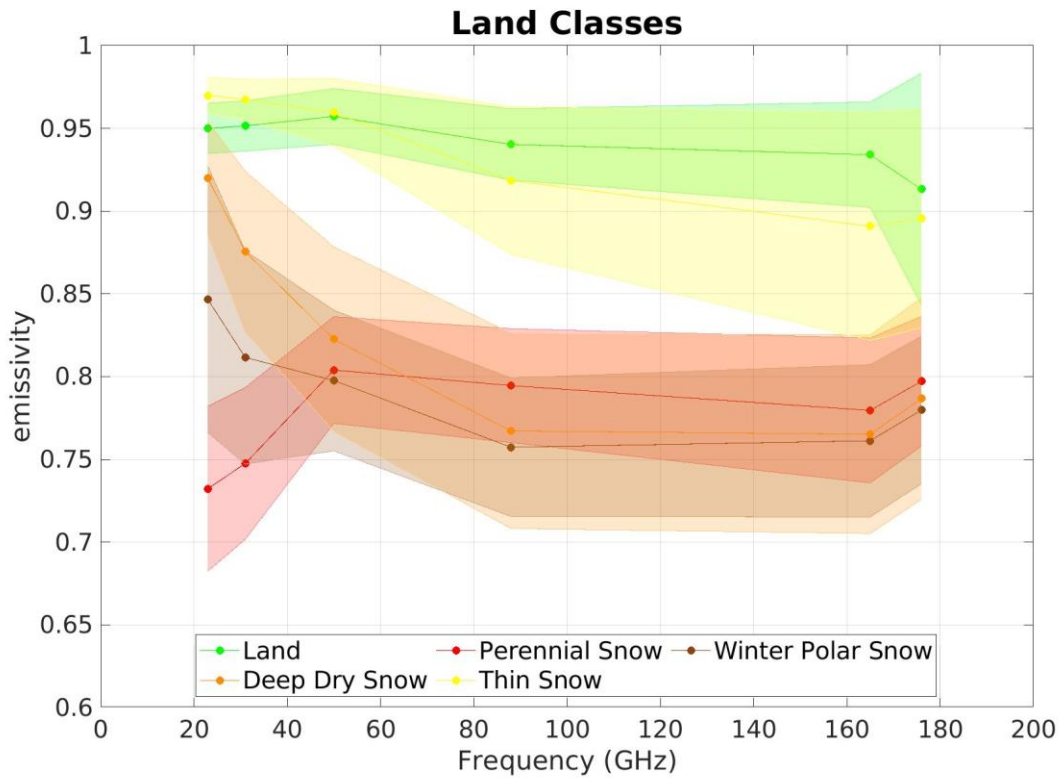


Figure 3: Sea Ice [Detection and classification](#): relationship between 31 GHz Pseudo-Emissivity (y-axis) and 23 GHz Pseudo-Emissivity (x-axis). The color represents the mean AutoSnow sea ice percentage within each bin (top [panel](#)), the observation occurrence (center [panel](#)), and the PESCA classification ([Multi-Layer \(ML\), Broken and New sea ice](#)) with the Nearest Neighbor markers (bottom [panel](#)).



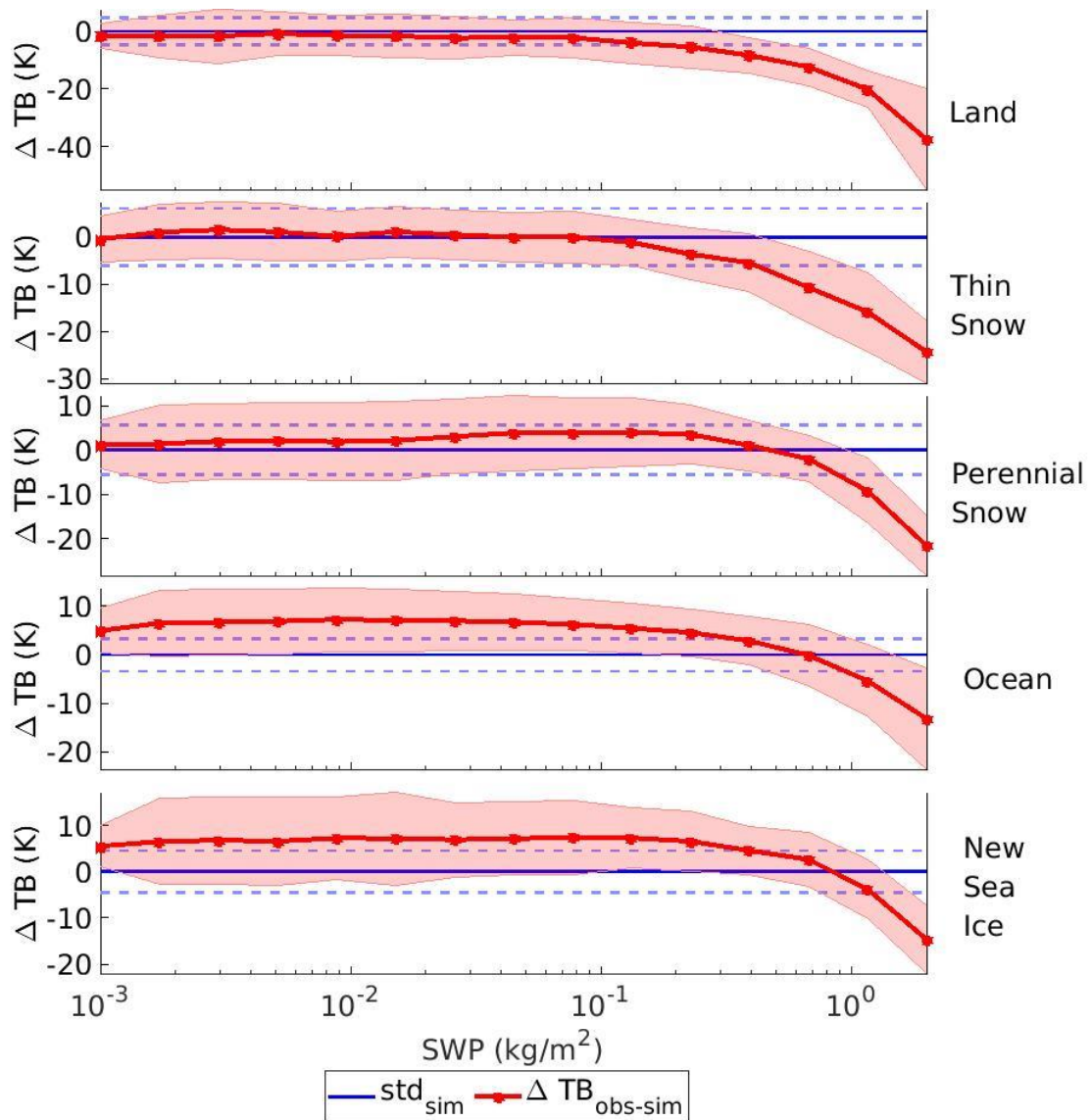
959
960
961
962

Figure 4: Emissivity Spectra for PESCA Sea Classes. The continuous lines represent the mean values of the emissivity while the shaded areas represent the standard deviation calculated at the ATMS reference frequencies (23.8 GHz, 31.4 GHz, 50.3 GHz, 88.2 GHz, 165.5 GHz, and 183.3 ±7 GHz) represented by the dots.



963
964
965

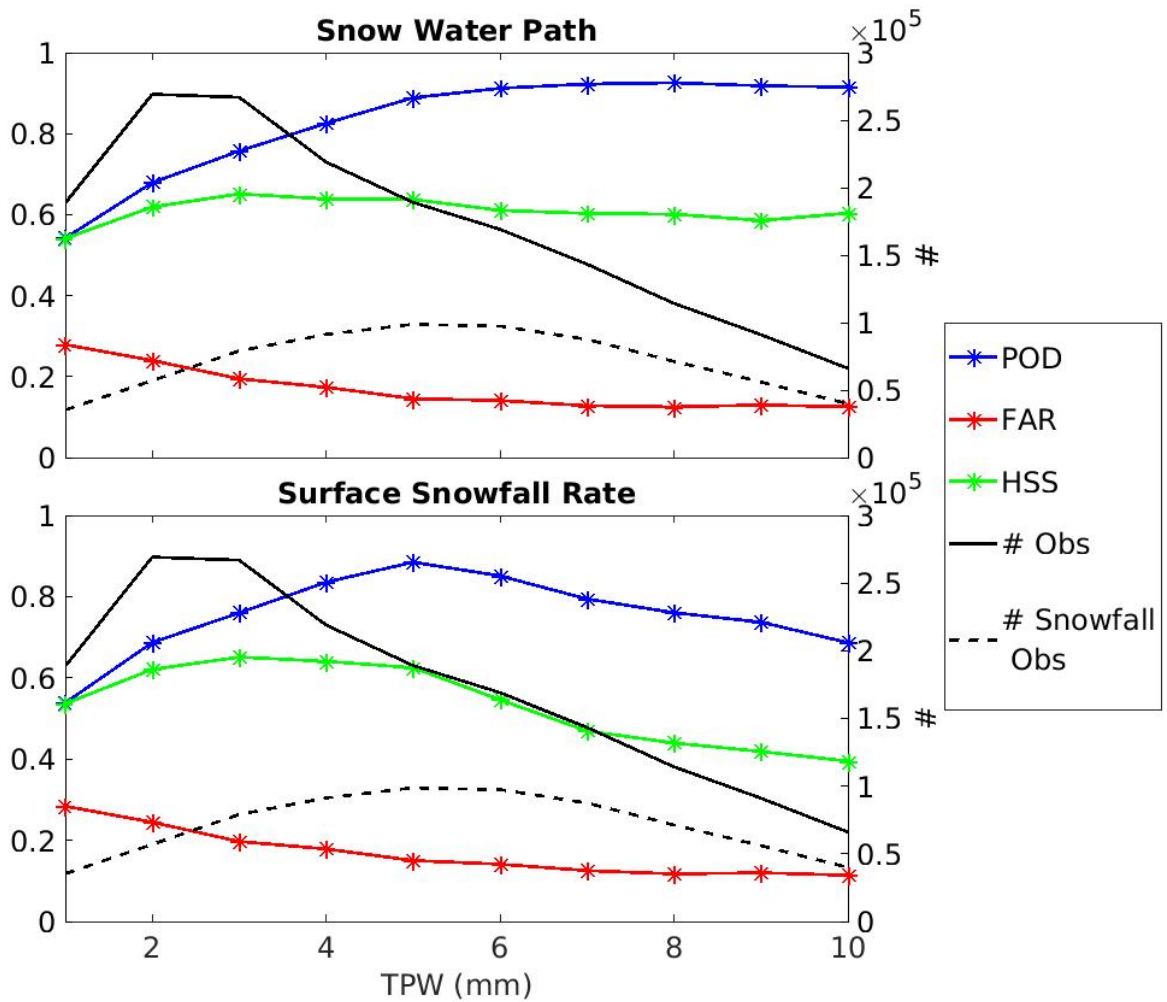
Figure 5: Same as Figure 4 but for PESCA Land Classes.



966
 967
 968
 969
 970

Figure 6: 165.5 GHz Snowfall Signature at 165.5 GHz as a function of SWP for three Land five PESCA surface Classes classes. The red line and shaded areas represent the mean values and standard deviations of $\Delta TB_{obs-sim}$ (i.e., the snowfall signature) while the blue lines are centered on the estimated bias and standard deviation of $\Delta TB_{obs-sim}$ in clear sky conditions for the corresponding PESCA surface class.

971



972

973

974

975

976

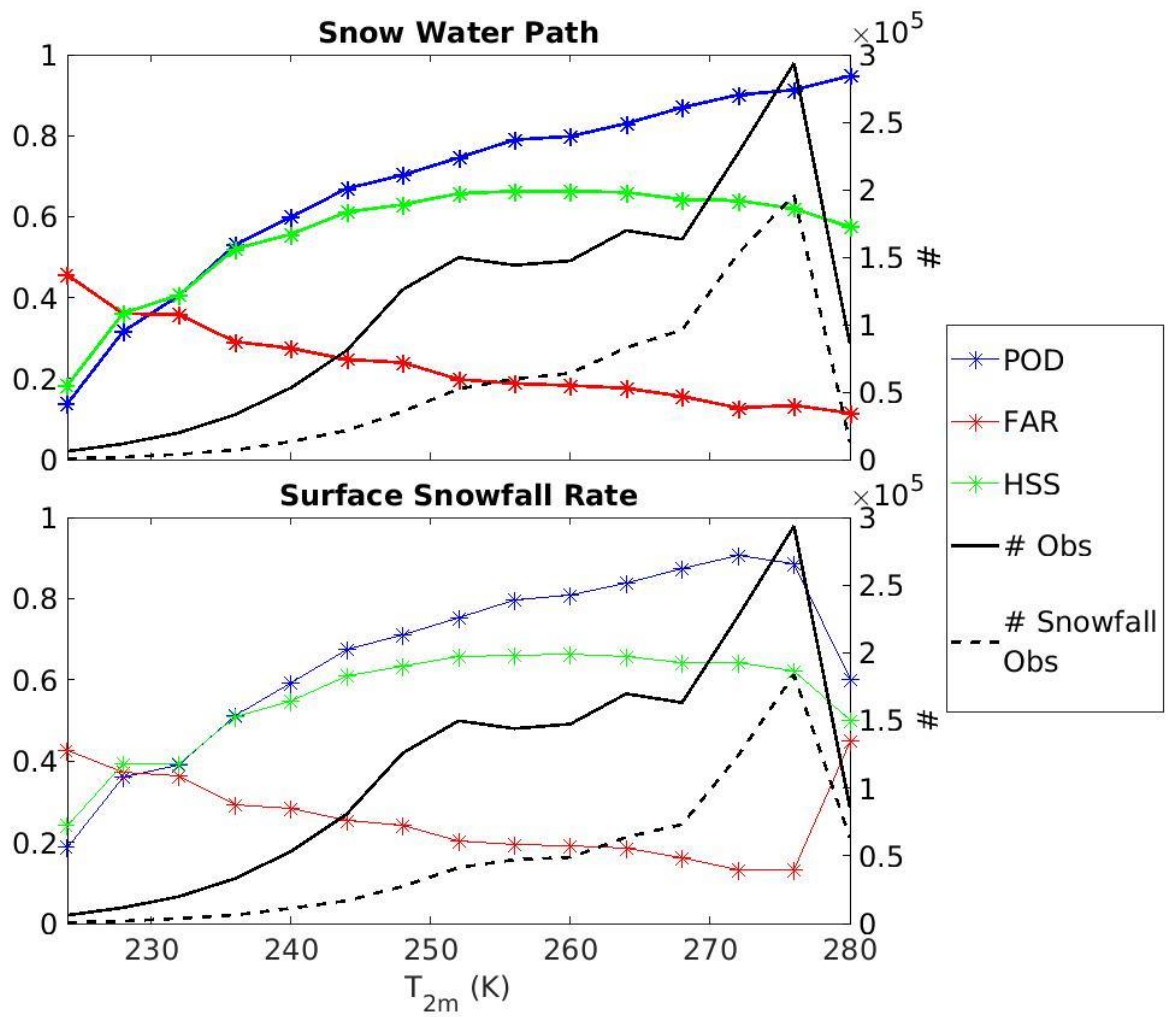
977

978

979

980

Figure 7-: Dependence of HANDEL-ATMS SWP and SSR Detection Performances detection statistical scores on TPW. Each star represents the statistical score value for different bins 1-mm t bin of TPW. The left y-axis reports POD, FAR and HSS vales values, while the right y-axis reports the total number of total and snowfall observations in the validation dataset. POD-tot, FAR-tot and HSS-tot (dotted lines) represent the statistical scores estimated on the total dataset (values reported in Table 2).

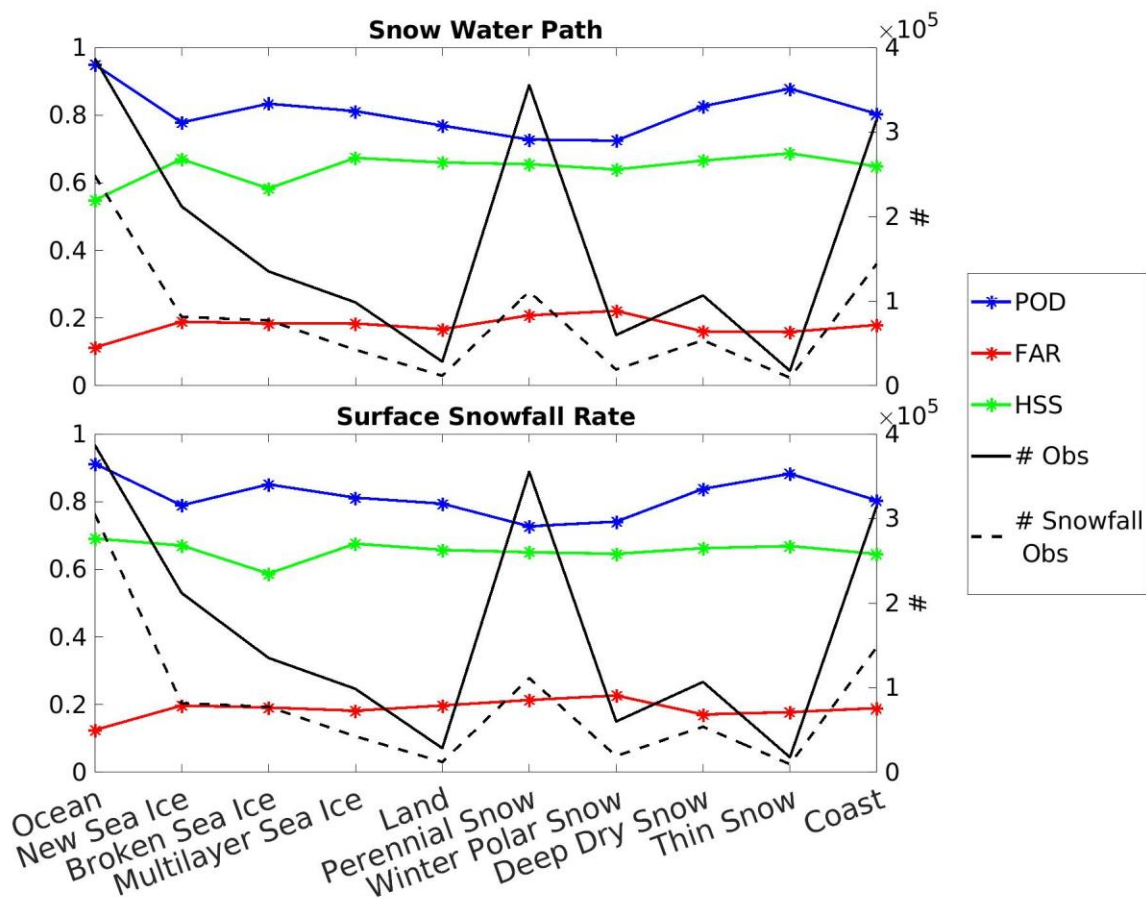


981

982

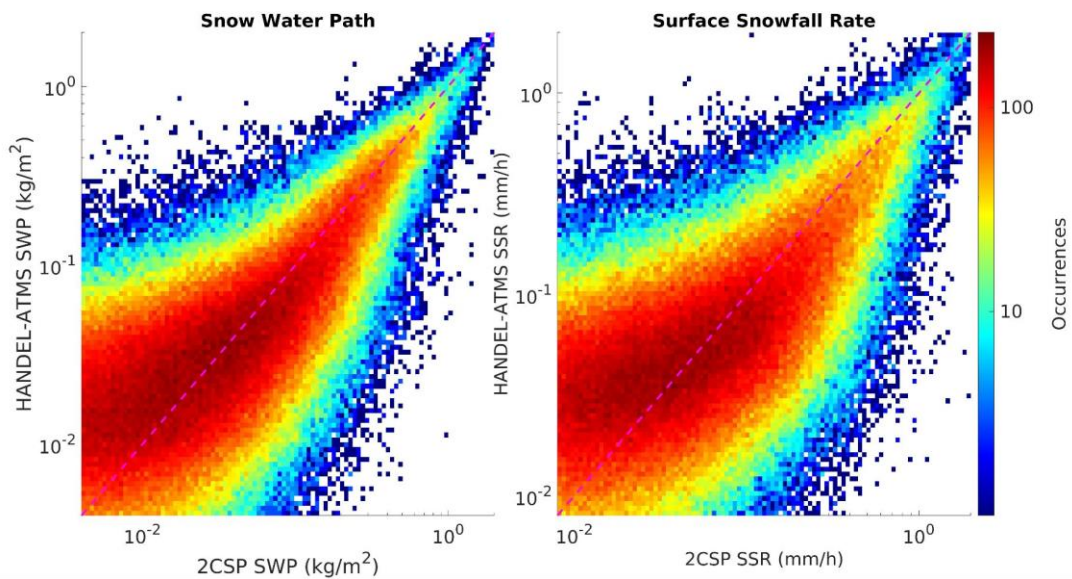
Figure 8: Same as Figure 7 but for $-T_{2m}$ bins.

983



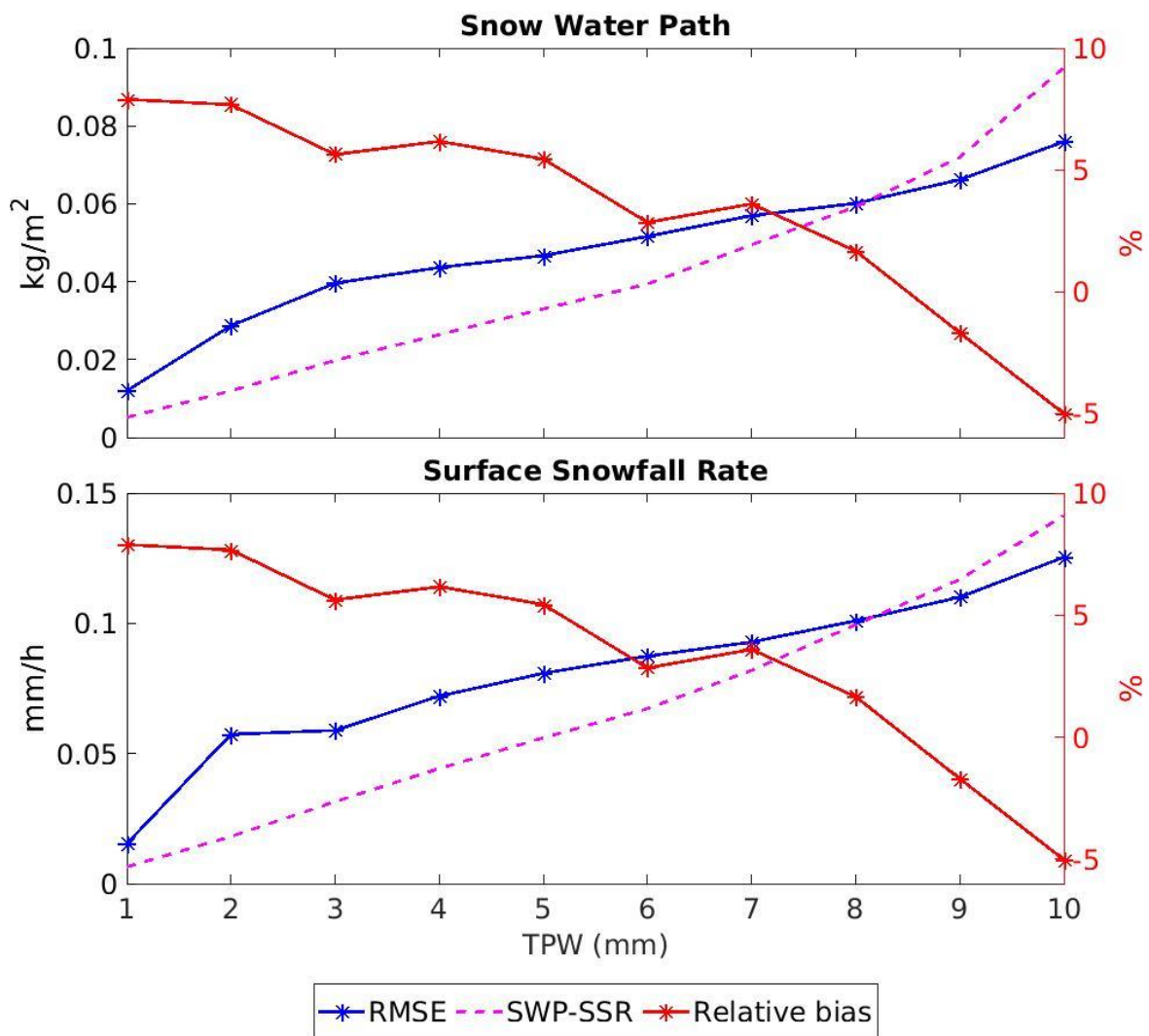
984
985
986
987

Figure 9: Same as Figure 7 but for PESA surface classes. Each star represents the value of the statistical score for each surface category.



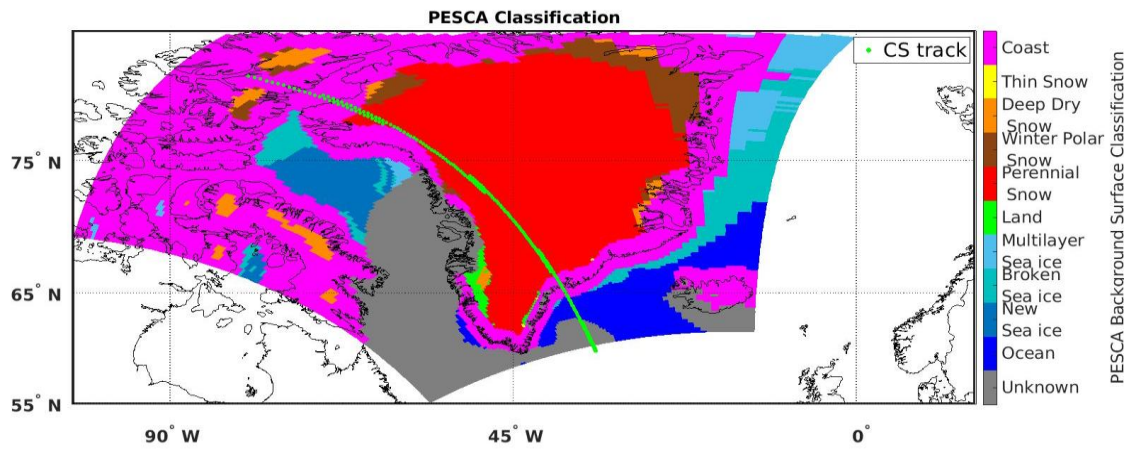
988
989
990
991
992
993

Figure 10: 2D Histogram reporting HANDEL-ATMS SWP (left) and SSR (right) estimation (y-axis) and 2CSP- estimation (x-axis). The colorbar represents the observation-number of observations for each HANDEL-ATMS/2CSP bin. The violet dashed line represents the bisector.



994
995
996
997
998
999

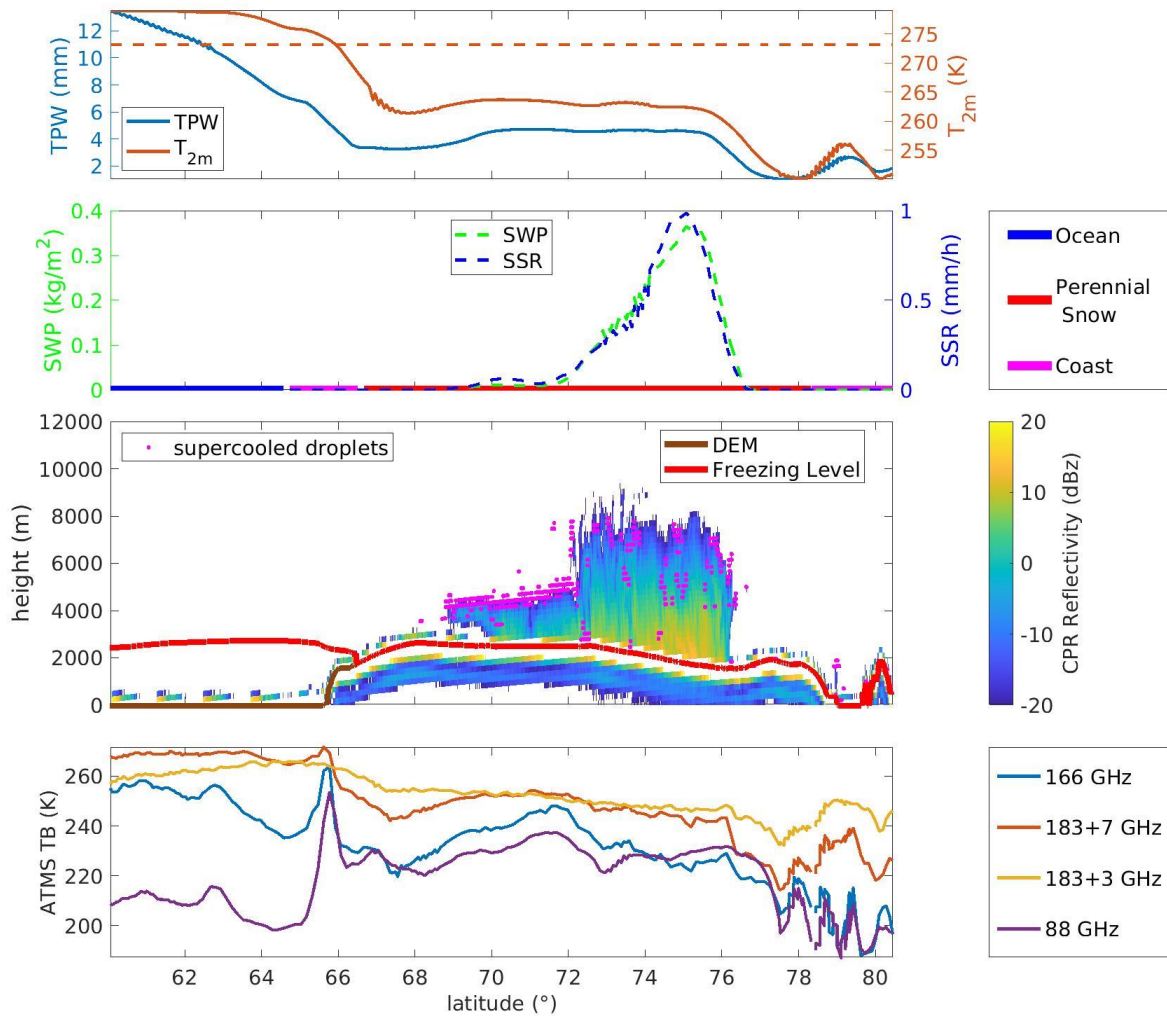
Figure 11: Dependence of HANDEL-ATMS SWP and SSR estimation on TPW. Each star represents the value of the statistical score for different 1-mm TPW bins. The left y-axis reports the RMSE and the mean intensity SWP and SSR value for each 1-mm TPW bin, while the right y-axis reports the relative bias, calculated as the ratio between the bias and the SWP/SSR mean value for each bin.



1000
 1001
 1002
 1003
 1004
 1005

[Figure 12: Greenland - 2016/04/24 - PESCA-ATMS overpass is between 14:54 UTC and 14:58 UTC, while the CPR overpass is between 15:05 UTC and 15:12 UTC. Map of the PESCA Background Surface Classification. The green dotted line represents the CloudSat track.](#)

1006



1007

1008

1009

1010

1011

1012

1013

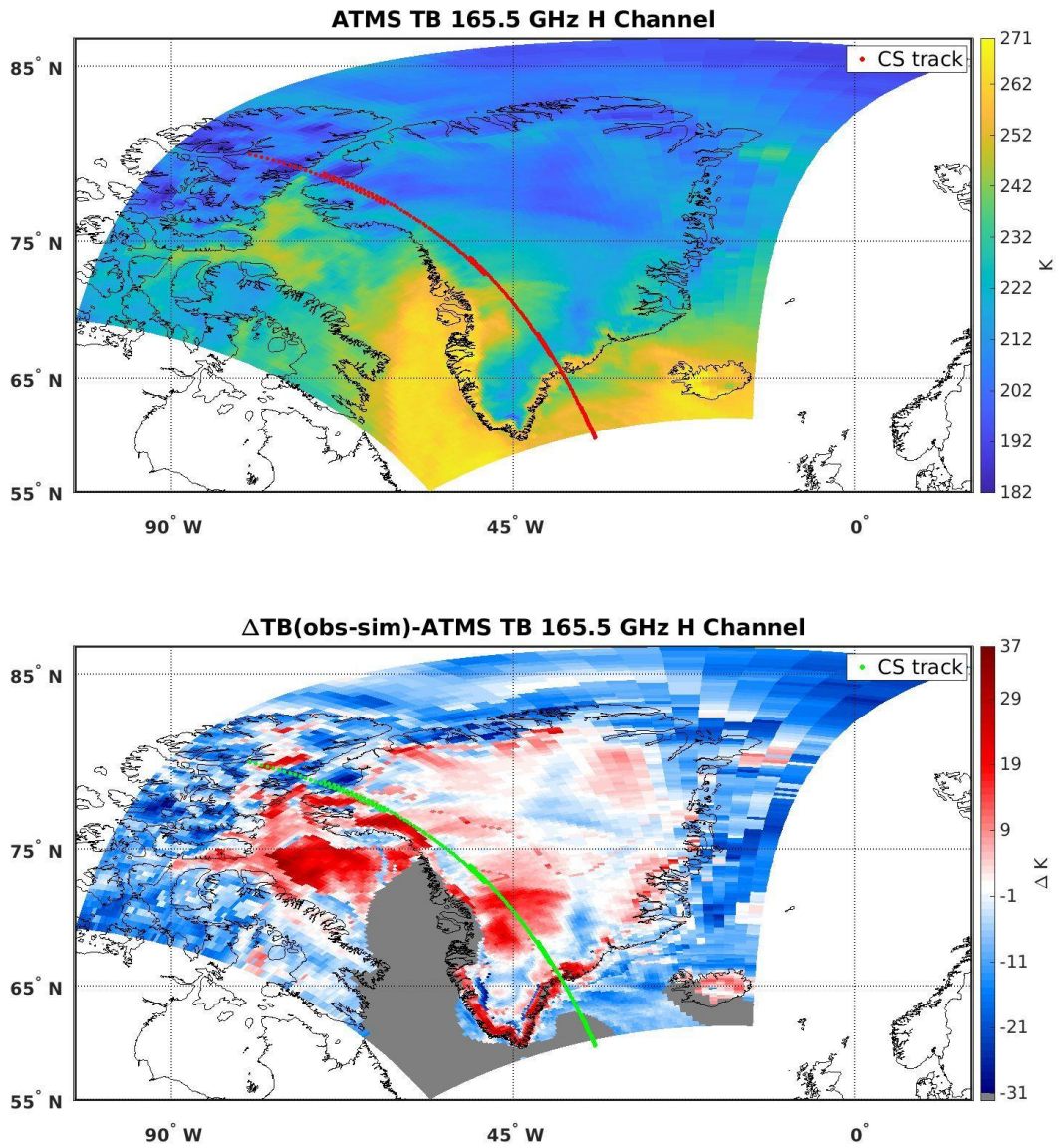
1014

1015

1016

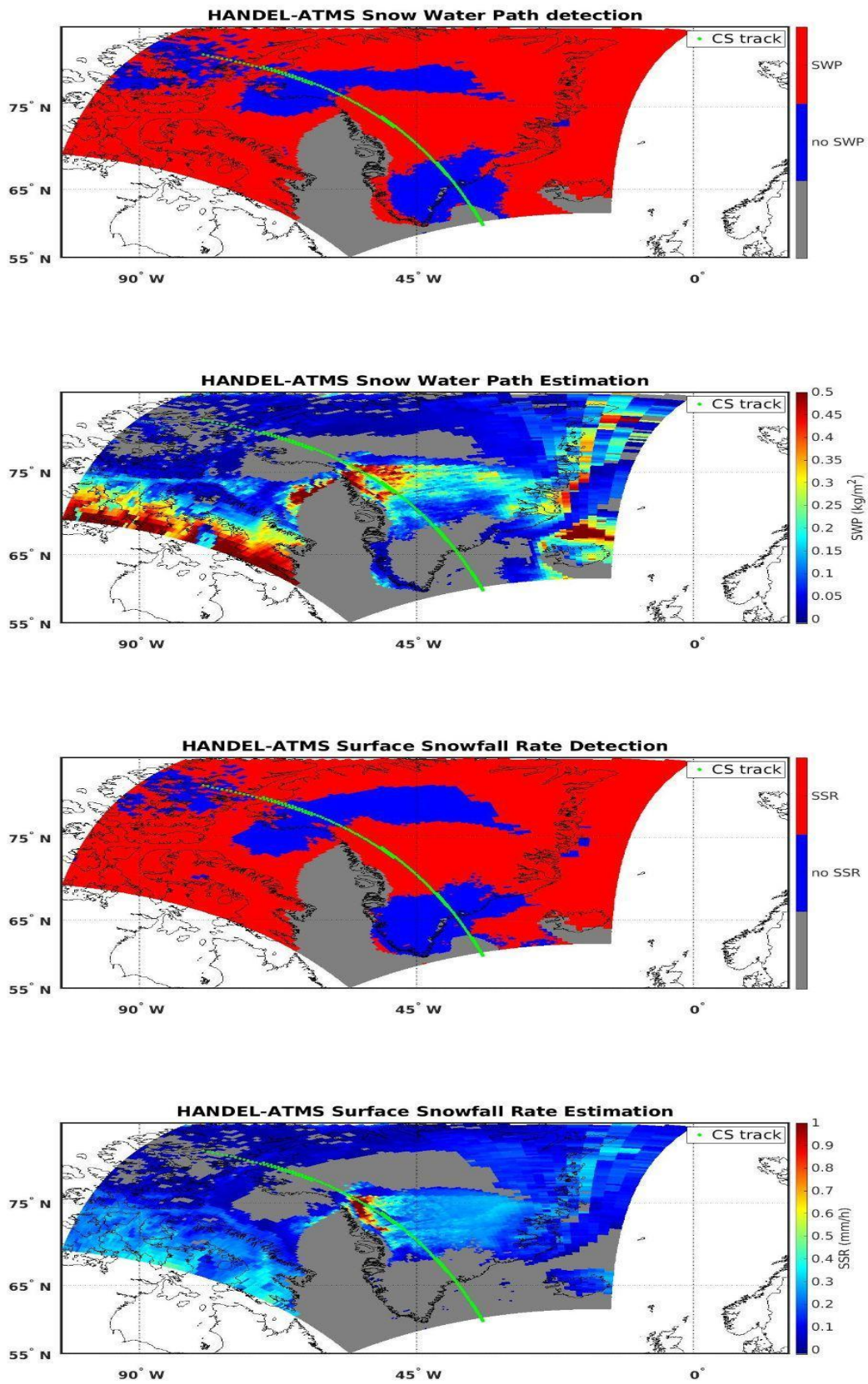
Figure 4413: Greenland - 2016/04/24 - Synopsis along CloudSat Track. The first panel shows the ECMWF TPW and T_{2m} values along the CloudSat track. In the second panel, the 2CSP SWP (left) and the SSR (right) values are reported, besides, and the PESCA classification along CloudSat track. In the third panel, the CPR reflectivity (values are reported in the colorbar below), on the right, and supercooled water droplets detected by DARDAR (magenta points) are shown. Also the Digital Elevation Model (brown line) and the ECMWF Freezing Level (red line) along CloudSat track are reported. In the bottom panel, the observed ATMS TBs of the main-high-frequency channels (88 GHz, 166 GHz, 183+3 GHz, 183+7 GHz) along CloudSat track are shown.

1017
1018
1019
1020
1021
1022
1023



1024
1025
1026
1027
1028
1029

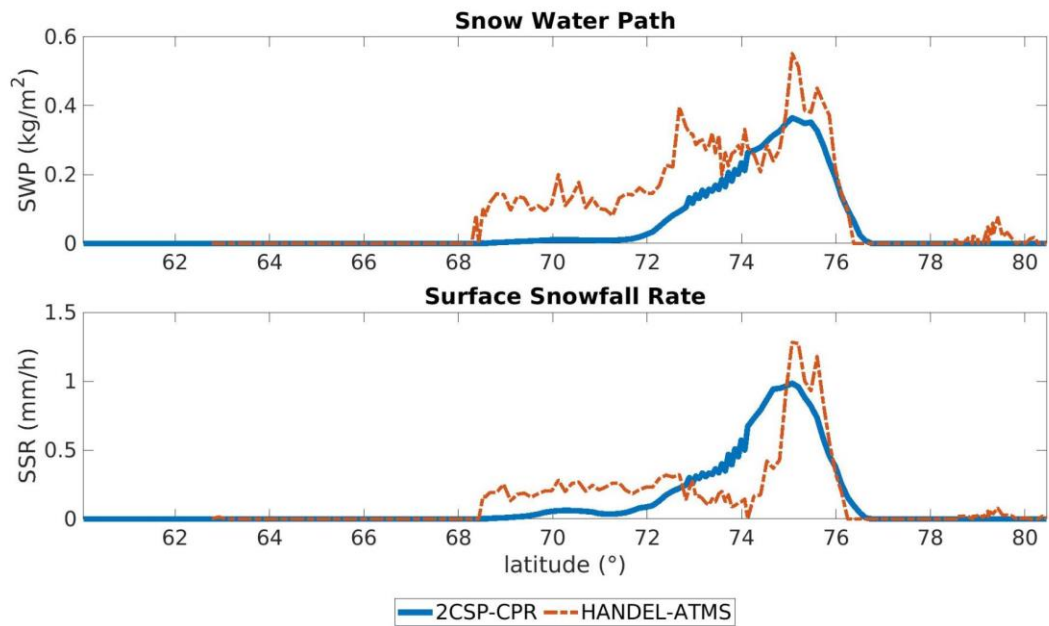
Figure 4214: Greenland - 2016/04/24 - 165 GHz Channel measured TB ($T_{B_{\text{obs}}}$) (top panel) and the deviation of $T_{B_{\text{obs}}}$ from the simulated clear-sky TBs ($\Delta(T_{B_{\text{obs}}-\text{sim}})$) (bottom panel). The red dotted line (top panel) and the green dotted line (bottom panel) represent the CloudSat track.



1030
 1031
 1032
 1033

Figure 4315: Greenland - 2016/04/24 - Maps of the HANDEL-ATMS module's output: the SWP detection mask (top panel), the estimated SWP (kg m^{-2}) (second panel), the SSR detection mask (third panel), the estimated SSR (mm h^{-1}) (bottom panel). The green dotted lines (bottom panel) represent the CloudSat track.

1034
1035
1036



1037

1038

Figure 4416: Greenland - 2016/04/24 - Comparison between CPR 2C-SNOW-PROFILE and HANDEL-ATMS SWP and SSR estimates along the CloudSat track.

1039

1040

1041

1042

1043

Tables

1044

1045

1046

	OCEAN MODULE	LAND MODULE
POD	0.99	0.98
FAR	0.01	0.01
HSS	0.98	0.72

1047

Table 1: PESCA Overall [Statistics](#) Scores

1048

1049

1050
1051

Class	n clusters	accuracy	165.5 GHz RMSE (K)	165.5 GHz NRMSE%	Predictor Set
Ocean	2	0.9	3.37	44	$P_{surf} - TPW - T_{2m}$
New Sea Ice	3	0.74	4.52	48	SI - T_{2m} - $-P_{surf}$ - ratio - jd - pem ₂₃
Broken Sea Ice	16	0.56	5.34	41	pem ₂₃ - TPW - SI - $-P_{surf}$
Multilayer Sea Ice	9	0.53	4.38	34	pem ₃₁ - SI - TPW - T_{2m} - pem ₂₃ - $-P_{surf}$
Land	2	0.87	4.57	52	DEM - jd - TPW
Perennial Snow	8	0.65	5.98	54	pem ₂₃ - jd - SI - pem ₃₁ - lat
Winter Polar Snow	5	0.76	5.87	37	pem ₃₁ - SI - lat - H_{sol} - pem ₃₁ - jd
Deep Dry Snow	15	0.34	6.77	45	SI - pem ₃₁ - ratio
Thin Snow	3	0.78	6.03	39	SI - ratio - lat
Coast	13	0.43	6.80	44	SI - pem ₂₃ - pem ₃₁ - DEM - T_{2m}

1052 **Table 2: Classification Refinement - Parameters.**
1053

Predictor Set	POD	FAR	HSS
$\Delta TB_{obs-sim} + \text{ancillary parameters}$	0.75	0.29	0.48
$TB_{obs} + \text{ancillary parameters}$	0.81	0.18	0.65
$TB_{obs} + \text{environmental var} + \text{ancillary parameters}$	0.82	0.17	0.68
$TB_{obs} + \Delta TB_{obs-sim} + \text{ancillary parameters}$	0.84	0.16	0.69

1054 **Table 3: HANDEL-ATMS SSR Detection Performance: Statistical scores for different Predictor Sets**
1055

	POD	FAR	HSS
SWP	0.85	0.15	0.70
SSR	0.84	0.16	0.69

1056 **Table 4: HANDEL-ATMS detection Performance - SWP and SSR Detection Modules Statistical Scores**
1057

	RMSE	bias	R ²
SWP (kg m ⁻²)	0.047	0.001	0.72
SSR (mm h ⁻¹)	0.079	0.002	0.61

1058 **Table 5: HANDEL-ATMS Estimation Performance - SWP and SSR Estimation Module Error Statistics** 
1059

1060
1061
1062

	POD		FAR	
	SLALOM-CT	HANDEL-ATMS	SLALOM-CT	HANDEL-ATMS
TPW<10 mm T _{2m} <280 K (*)	0.82	0.84	0.19	0.16
TPW<5 mm T _{2m} <250 K	0.64	0.68	0.28	0.23
TPW<3 mm T _{2m} <240 K	0.45	0.54	0.33	0.28

1063 **Table 7:** Comparison between HANDEL-ATMS and SLALOM-CT detection Performances for Different
1064 Environmental Conditions (* HANDEL-ATMS working limits).

1065
1066

1067 In this document, changes to Article:

1068 amt-2023-94

1069 Title: The High Latitude snowfall Detection and Estimation algorithm for ATMS
1070 (HANDEL-ATMS): a new algorithm for the snowfall retrieval at high latitudes

1071 Author(s): Andrea Camplani et al.

1072 MS type: Research article

1073

1074 because of the referees' comments are shown.

- 1075
- 1076 • The changes reported in the responses to the referees were introduced.
 - 1077 • The text has been modified and deeply revised, simplifying some sentences and
1078 reducing not relevant parts in the methodology section, according to referee # 2
1079 suggestions.
 - 1080 • 2 figures have been added (Figure 9, Figure 11), all Captions have been modified
1081 accordingly.
 - 1082 • Figures 2, 6, 7, 8, 11 (now 13), and 14 (now 16) have been modified.
 - 1083 • Table 6 has been removed and replaced with Figure 9; all Captions have been modified
1084 accordingly.

1084

1085